# Optical and Microphysical Characterization of Biomass-Burning and Industrial-Pollution Aerosols from Multiwavelength Lidar and Aircraft Measurements

**Article** *in* Journal of Geophysical Research Atmospheres · November 2002

DOI: 10.1029/2000JD000202 · Source: OAI

CITATIONS
235

READS
207

**11 authors**, including:

Detlef Müller
University of Hertfordshire
**267** PUBLICATIONS **13,367** CITATIONS
SEE PROFILE

Christine Böckmann
Universität Potsdam
**127** PUBLICATIONS **1,824** CITATIONS
SEE PROFILE

Volker Matthias
Helmholtz-Zentrum Hereon
**169** PUBLICATIONS **4,977** CITATIONS
SEE PROFILE

Manfred Wendisch
University of Leipzig
**415** PUBLICATIONS **10,762** CITATIONS
SEE PROFILE

# Optical and microphysical characterization of biomass-burning and industrial-pollution aerosols from multiwavelength lidar and aircraft measurements

Ulla Wandinger,[1] Detlef Müller,[1] Christine Böckmann,[2] Dietrich Althausen,[1] Volker Matthias,[3] Jens Bösenberg,[3] Volker Weiß,[4] Markus Fiebig,[4] Manfred Wendisch,[1] Andreas Stohl,[5] and Albert Ansmann[1]

Received 28 November 2000; revised 7 June 2001; accepted 11 June 2001; published 18 September 2002.

[1] During the Lindenberg Aerosol Characterization Experiment (LACE 98) simultaneous measurements with ground-based and airborne lidars and with two aircraft equipped with aerosol in situ instrumentation were performed. From the lidar measurements, particle backscatter coefficients at up to eight wavelengths between 320 and 1064 nm and particle extinction coefficients at 2–3 wavelengths between 292 and 532 nm were determined. Thus, for the first time, an extensive set of optical particle properties from several lidar platforms was available for the inversion into particle microphysical quantities. For this purpose, two different inversion algorithms were used, which provide particle effective radius, volume, surface-area, and number concentrations, and complex refractive index. The single-scattering albedo follows from Mie-scattering calculations. The parameters were compared to the ones from airborne measurements of particle size distributions and absorption coefficients. Two measurement cases were selected. During the night of 9–10 August 1998 measurements were taken in a biomass-burning aerosol layer in the free troposphere, which was characterized by a particle optical depth of about 0.1 at 550 nm. Excellent agreement between remote-sensing and in situ measurements was found. In the center of this plume the effective radius was approximately 0.25 $\mu$m, and all methods showed rather high complex refractive indices, ranging from 1.56–1.66 in real part and from 0.05–0.07$i$ in imaginary part. The single-scattering albedo showed low values from 0.78–0.83 at 532 nm. The second case, taken on 11 August 1998, presents the typical conditions of a polluted boundary layer in central Europe. Optical depth was 0.35 at 550 nm, and particle effective radii were 0.1–0.2 $\mu$m. In contrast to the first case, imaginary parts of the refractive index were below 0.03$i$. Accordingly, the single-scattering albedo ranged from 0.87–0.95. *INDEX TERMS:* 0305 Atmospheric Composition and Structure: Aerosols and particles (0345, 4801); 0345 Atmospheric Composition and Structure: Pollution-urban and regional (0305); 0365 Atmospheric Composition and Structure: Troposphere-composition and chemistry; 0368 Atmospheric Composition and Structure: Troposphere-constituent transport and chemistry; *KEYWORDS:* Multiwavelength lidar, inversion, LACE 98, aerosol optical properties, aerosol microphysical properties

**Citation:** Wandinger U., D. Müller, C. Böckmann, D. Althausen, V. Matthias, J. Bösenberg, V. Weiß, M. Fiebig, M. Wendisch, A. Stohl, and A. Ansmann, Optical and microphysical characterization of biomass-burning and industrial-pollution aerosols from multiwavelength lidar and aircraft measurements, *J. Geophys. Res.*, *107*(D21), 8125, doi:10.1029/2000JD000202, 2002.

## 1. Introduction

[2] Lidar has proven to be a very effective tool in aerosol characterization experiments [e.g., *Ferrare et al*., 1998a, 1998b; *Redemann et al*., 1998, 2000; *Ansmann et al*., 2000, 2001; *Müller et al*., 2000b, 2001a, 2001b]. Lidar measurements of particle optical properties with high resolution in time and space give detailed information on occurence, extent, and development of aerosol structures. From the independent detection of particle extinction and backscattering properties by the use of the Raman-lidar technique [*Ansmann et al*., 1992], an optical characterization of aerosols is possible [e.g., *Ferrare et al*., 1998a]. The extinction-to-backscatter, or lidar, ratio obtained with this technique contains information on the aerosol type, since it depends on the index of refraction and on the size of the particles [*Ackermann*, 1998]. In another approach the spectral dependence of aerosol backscattering was used to classify aerosol types from lidar measurements at three wavelengths [*Sasano and Browell*, 1989]. Only few efforts have been made so far to infer concrete physico-chemical properties of tropospheric aerosol particles such as their size, concentration, or index of refraction from lidar data. *Ferrare et al*. [1998a] and *Redemann et al*. [1998, 2000] combined lidar measurements

[1]Institute for Tropospheric Research, Leipzig, Germany.
[2]Institute for Mathematics, University of Potsdam, Potsdam, Germany.
[3]Max Planck Institute for Meteorology, Hamburg, Germany.
[4]German Aerospace Center, Oberpfaffenhofen, Germany.
[5]Technical University of Munich, Freising, Germany.


0148-0227/02/2000JD000202$09.00

and in situ observations from aircraft to obtain information on refractive index and single-scattering albedo.

[3] At the Institute for Tropospheric Research (IfT) a six-wavelength lidar, that combines Raman and multiwavelength observations [*Althausen et al*., 2000], is used in conjunction with an inversion algorithm to obtain a comprehensive set of particle properties, namely, the effective radius, number, surface-area, and volume concentrations, complex refractive index, and single-scattering albedo. The possibility to invert these parameters from the multiwavelength measurements has only recently been successfully demonstrated [*Müller et al*., 1998, 1999a, 1999b, 2000a; *Böckmann*, 2001]. The great potential of this approach to investigate the aerosol radiative forcing by delivering the necessary information on particle properties for radiative-transfer calculations on a height- and time-resolved basis has been shown [*Müller et al*., 2000a, 2000b, 2001a, 2001b]. Extensive data sets were obtained with the six-wavelength lidar during the Second Aerosol Characterization Experiment 2 (ACE 2, Portugal, June/July 1997), the Lindenberg Aerosol Characterization Experiment (LACE 98, Germany, July/August 1998), and the Indian Ocean Experiment (INDOEX, Maldives, February 1999 to March 2000).

[4] However, very few comparisons with other measurements to validate the multiwavelength-lidar approach could be performed so far [*Müller et al*., 2000a]. Also, the two inversion algorithms developed at IfT [*Müller et al*., 1999a, 1999b, 2000a] and at the Institute for Mathematics of the Potsdam University (IMP) [*Böckmann*, 2001] were not yet compared. LACE 98 (Lindenberg, Germany, 52.2°N, 14.1°E) offered for the first time the opportunity to fill this gap by using combined remote-sensing and in situ observations [*Ansmann et al*., 2002]. An extended set of optical data was available from simultaneous measurements with several lidar instruments, which are capable of determining particle backscatter and extinction coefficients in a wide wavelength range. Never before was so much aerosol information available from lidar measurements. Two airplanes were operated to probe the vertical air column, that was simultaneously observed with the ground-based lidar instruments. The fast-flying Falcon normally descended from the tropopause to the lower boundary layer in several flight legs, while the slow-flying Partenavia with a ceiling of 4 km flew slow ascents and descents in the boundary layer and the lower free troposphere. The aircraft were equipped with a variety of aerosol sensors, the Falcon also with a downward looking lidar. Seven joint missions and five single-aircraft flights on nine different days were performed during LACE 98.

[5] In this paper, we discuss in detail two selected cases for which closure studies concerning aerosol optical and microphysical properties were carried out. In the first case, a large-scale aerosol layer in the free troposphere, which originated from forest fires in northern Canada, was investigated. Simultaneous measurements with three ground-based lidars and the lidar on board the Falcon were taken. Particle backscatter coefficients at eight wavelengths and particle extinction coefficients at three wavelengths could be determined. The two inversion algorithms were applied to invert particle microphysical properties from the multiwavelength information. The results are compared to the parameters measured with airborne in situ instruments aboard the Falcon. This case was of special interest, not only because a rare and interesting event of intercontinental aerosol transport could be studied, but also because very low humidity values in the aerosol layer gave the opportunity for a comparison of lidar-derived parameters and in situ data without applying a humidity-growth correction to the airborne measurements of dry particles. Furthermore, the measurements were performed at nighttime, so that the lidar measurements were less disturbed by background noise, which is especially important for the retrieval of extinction data from Raman measurements.

[6] The second measurement deals with a polluted boundary layer. This case was chosen, because it represents a typical pollution situation in central Europe. The air was advected from highly industrialized regions to the field site. Particle backscatter coefficients at seven wavelengths and particle extinction coefficients at three wavelengths were measured with two ground-based lidars. The inversion results from the two algorithms are compared to parameters measured in situ aboard the Partenavia. The aircraft measurements were, however, made several hours prior to the lidar measurements, since the Partenavia is not allowed to fly in darkness.

[7] In section 2 the different lidar instruments and the airborne in situ sensors are described. The inversion methods are discussed in section 3, and the results for the two measurement cases are presented in section 4. Section 5 gives the conclusions.

## 2. Instrumentation and Data Processing

### 2.1. Lidars

[8] Data of four sophisticated ground-based and airborne lidars were used. Three of the four instruments detect pure molecular scattering, i.e., Raman or Rayleigh backscatter signals, from which particle extinction coefficients can be determined independently of particle backscatter coefficients. Key instrument is the multiwavelength lidar of the IfT, which has been especially developed for the study of tropospheric aerosols. It yields information on aerosol backscattering at six wavelengths between 355 and 1064 nm and on aerosol extinction at 355 and 532 nm. Measurements of backscattering and extinction at additional wavelengths could be provided by the combined UV ozone/Raman lidar (either extinction at 292 nm and backscattering at 320 nm or extinction and backscattering at 351 nm) and the IR water-vapor lidar (backscattering at 729 nm) of the Max Planck Institute for Meteorology, Hamburg (MPI). The high-spectral-resolution lidar (HSRL) of the German Aerospace Center (Deutsches Zentrum für Luft- und Raumfahrt (DLR)) on board the Falcon was flown for the first time during LACE 98 and is the first airborne lidar of this kind. Aerosol backscatter coefficients at 355, 532, and 1064 nm and the aerosol extinction coefficient at 532 nm are measured with this system. In the following subsections, the main technical parameters of the four lidars and the data processing are described.

#### 2.1.1. IfT Multiwavelength Lidar

[9] The IfT multiwavelength lidar emits laser pulses at 355, 400, 532, 710, 800, and 1064 nm simultaneously with a repetition rate of 30 Hz. Two Nd:YAG and two dye lasers are used as radiation sources. Pulse energies are of the order of 500, 250, and 80 mJ in the case of the Nd:YAG wavelengths at 1064, 532, and 355 nm, respectively, and around 10, 3, and 1.5 mJ for the dye wavelengths at 710, 800, and 400 nm, respectively. With a beam-combining unit, which consists of dichroic and polarizing mirrors, all six laser beams are aligned onto one optical axis. The laser beam is expanded tenfold and emitted into the

atmosphere via a turnable mirror, which allows operation under zenith angles from −90° to +90°.

[10] Backscattered light is sampled with a 0.53-m Cassegrain telescope. In 11 channels the elastic backscatter signals at the six emitted wavelengths, the cross-polarized signal at 710 nm, and the Raman signals of nitrogen at 387 and 607 nm and of water vapor at 660 nm are detected. Signals are selected with dichroic and polarizing beamsplitters and narrowband interference filters. Photomultiplier tubes (PMTs) are used as detectors at all wavelengths. Whereas for the elastic backscatter signals the analog PMT output is digitized (12 bit, 10 MHz) and stored, the Raman signals and part of the corresponding elastically scattered light at the primary wavelengths of 355 and 532 nm are detected in the photon-counting mode. PMTs, discriminators, and photon counters operate at 300 MHz. A detailed description of the IfT multiwavelength lidar is given by *Althausen et al*. [2000].

### 2.1.2. MPI UV Lidar

[11] The MPI UV lidar is based on an excimer laser, which can be operated either with XeF at a wavelength of 351 nm or with KrF at 248 nm. The pulse energies are 40 and 200 mJ, respectively, at a repetition rate of 10 Hz. With KrF filling, the lidar works as a combined ozone differential-absorption/Raman lidar. Stimulated Raman scattering from deuterium, which is stored in a gas cell under a pressure of 40 bar, converts the laser radiation from 248 nm to 268, 292, and 320 nm with pulse energies of about 30, 15, and 5 mJ, respectively. The laser beam is threefold expanded and then vertically emitted into the atmosphere. Signals are simultaneously detected with two receiver telescopes of 0.15- and 0.40-m diameter for measurements in height ranges from 300 to 2500 m and from 1200 to 9000 m, respectively. In this way, signal dynamics is reduced and the effect of incomplete overlap between laser beam and receiver field of view (see subsection 2.1.5) is minimized.

[12] In XeF operation the elastic backscatter signal at 351 nm and the Raman backscatter signal from nitrogen at 382 nm are measured. In KrF operation, the lidar receives three elastic wavelengths at 268, 292, and 320 nm and two Raman signals at either 286 nm (Raman scattering from nitrogen for primary radiation at 268 nm) or 306 nm (Raman scattering from nitrogen for primary radiation at 292 nm). The wavelength separation is done with dichroic mirrors in XeF operation and with a grating spectrometer in KrF operation. After passing narrowband interference filters, the signals are detected with PMTs. For the elastic backscatter signals the analog PMT output is amplified, digitized (12 bit, 10 MHz), and stored on a computer. To detect the Raman signals, PMTs in photon-counting mode, discriminators, and a dual-channel 700-MHz photon-counting board are used. The MPI UV lidar is described in more detail by *Matthias* [2000].

### 2.1.3. MPI Water-Vapor Lidar

[13] The MPI water-vapor DIAL (differential-absorption lidar) emits two wavelengths in the 730-nm region, one of which is at the center of a water-vapor absorption line (on-line wavelength) and one is separated from the line by approximately 90 pm (off-line wavelength). Several on-line wavelengths of different strengths can be chosen. During LACE 98 the system was operated at 729 nm.

[14] The emitted wavelength is produced by a continuous-wave single-frequency Ti:sapphire laser. This laser is pumped with a frequency-doubled Nd:YVO laser. The Ti:sapphire laser serves as a seed laser for a flashlamp-pumped alexandrite ring laser, which delivers a pulse energy of 30 mJ at 20-Hz repetition rate. The on-/off-line frequencies required for the DIAL measurement are produced in the Ti:sapphire laser by applying a voltage on a pockels cell inside the resonator.

[15] The backscattered light is collected with a 0.4-m-diameter Cassegrain telescope, which covers a height range from 800 to 8000 m for the off-line wavelength. The detector system consists mainly of a narrowband interference filter for daylight-background suppression and an avalanche photodiode as a detector. The signal is amplified, digitized, and stored on a computer. For the aerosol backscatter measurements, the off-line signals are used only. A detailed description of the water-vapor DIAL can be found in *Wulfmeyer and Bösenberg* [1998].

### 2.1.4. Airborne High-Spectral-Resolution Lidar

[16] The HSRL of the DLR was designed for operation on board the research aircraft Falcon for nadir observation. It uses a Nd:YAG laser with a maximum pulse energy of 150 mJ at 532 nm and a repetition rate of 10 Hz. The pulsed Nd:YAG laser is injection-seeded for single-mode operation with a monolithic, diode-pumped, continuous-wave Nd:YAG laser. The frequency of the seed laser is stabilized to an iodine absorption line at 532.26 nm by use of a gas cell filled with iodine vapor.

[17] The backscattered photons are collected with a 0.35-m-diameter Cassegrain telescope. Dichroic beamsplitters and interference filters are used to select conventional elastic backscatter signals at the Nd:YAG wavelengths. Photomultiplier tubes in analog mode detect the signals at 355 and 532 nm, whereas an avalanche photodiode is applied at 1064 nm.

[18] The 532-nm signal is divided into three parts. A polarizing beamsplitter separates the parallel- and cross-polarized components first. The light, that has a polarization parallel to the polarization of the transmitter, is then divided into two equal parts. One part, that contains both the narrow-line particle backscattering and the Doppler-broadened molecular backscattering, is directly detected. The other one passes an iodine-vapor absorption cell of 8-cm length and a temperature of 315 K. For these parameters, the absorption line of iodine at the center wavelength of 532.26 nm leads to a suppression of the particle backscattering of approximately a factor of $10^3$, whereas, due to the absorption line width of 1.7 GHz, the wings of the molecular return with a Doppler width of 2.6 GHz at 293 K can pass the cell. Therefore the detector behind the absorption cell measures the molecular response mainly.

### 2.1.5. Lidar-Data Processing and Error Sources

[19] Spectral extinction and backscatter coefficients are determined from the lidar signals with three well-known methods. These methods are briefly explained in the following. Special attention is given to the error estimation and the synergy effects, which can be obtained by combining the information content derived from the different methods.

#### 2.1.5.1. Extinction Coefficients

[20] From the measured pure molecular lidar signals, i.e., nitrogen Raman signals in the case of the IfT multiwavelength lidar and the MPI UV lidar and Rayleigh signals in the case of the airborne HSRL, particle extinction coefficients at the respective wavelengths are calculated [*Ansmann et al*., 1990]. Appropriate averaging in space and time is necessary in order

to reduce signal noise, especially in the case of the weak Raman signals. In the 350/530-nm wavelength region the low signal-to-noise ratios allow Raman measurements throughout the troposphere only at nighttime. Below 300 nm, in the solar-blind region, daytime operation is possible, but the profiles are limited in range and accuracy because of ozone absorption, which has to be corrected for from the respective DIAL measurement in the case of the MPI UV lidar. The typical resolution of extinction measurements with Raman lidars is 30–60 min in time and 100–600 m in space. HSRL extinction profiles are acquired typically within 2 min with the same spatial resolution. The statistical error of the molecular signal of <5% reached by the averaging permits one to retrieve extinction coefficients with a statistical error of <10–20%, if a sufficient extinction of the signal of >0.05 $km^{-1}$ occurs. The detection limit is of the order of 0.005 $km^{-1}$.

[21] Because particle extinction coefficients are determined from a single molecular signal profile, measurements close to the lidar are biased by the incomplete overlap of laser beam and receiver field of view. In the case of measurements with large telescopes, this effect may prohibit extinction-coefficient determination up to distances of several kilometers from the lidar. To overcome this problem, two methods are applied. The MPI UV lidar is equipped with an additional small telescope, that is used for measurements in the near field (see subsection 2.1.2). For the IfT multiwavelength lidar the overlap function is experimentally determined and corrected for. Therefore, in both cases, measurements can start at a distance of 500–800 m from the lidar. The remaining error of the extinction coefficient because of the overlap effect is estimated to be <0.02 $km^{-1}$ for distances <2 km and is negligible above. Airborne HSRL measurements are performed in nadir geometry from flight levels above 8 km. Thus the overlap effect does not influence measurements in aerosol layers, that appear well below the airplane.

[22] Other systematic errors, which might result from uncertainties in the input parameters needed to evaluate the molecular signals [*Ansmann et al*., 1990, 1992], are negligible in the cases discussed here. Several radiosonde launches per day at the field site provided actual pressure and temperature profiles, from which Rayleigh-extinction and nitrogen-number-density profiles can be calculated with high accuracy. Also, the wavelength dependence of the aerosol extinction coefficient between the primary and the nitrogen Raman wavelengths can be estimated iteratively, because extinction measurements at several wavelengths were performed. Additional information on this input parameter was available from spectral optical-depth measurements with Sun and star photometers at the field site [*Ansmann et al*., 2002]. For the HSRL a wavelength correction is not necessary, because the molecular wavelength is close to the primary wavelength.

[23] In summary, the extinction-coefficient measurement is limited to relative errors of the order of 10–20% by the statistical uncertainty. Systematic errors of the order of <0.02 $km^{-1}$ mainly occur in the near field.

#### 2.1.5.2. Backscatter Coefficients (Raman Method)

[24] From the ratio of the elastic backscatter signals and the corresponding nitrogen Raman signals, backscatter coefficients are determined with the so-called Raman method [*Cooney et al*., 1969; *Melfi,* 1972; *Ansmann et al*., 1992]. Input parameter is the particle backscatter coefficient at a specific distance from the lidar. In order to minimize the influence of this reference value, it is usually set into a height region, where molecular scattering is much stronger than particle scattering. Appropriate regions of clear air can be identified from the extinction profiles derived before, but also from the signal-ratio profile itself. The systematic error of the backscatter coefficient caused by an incorrect estimate of the reference value is usually <0.0001 $km^{-1}sr^{-1}$. The statistical error of the backscatter coefficient because of signal noise is reduced to <5–10%, if similar averaging in time and space is applied as in the extinction-coefficient retrieval, and for absolute particle backscatter coefficients of >0.0002 $km^{-1}sr^{-1}$. Profiles of molecular extinction and backscatter coefficients at the primary and at the Raman wavelengths needed in the evaluation were again calculated from actual radiosonde data and do not lead to significant errors. In the Raman method the overlap effect is cancelled out because the ratio of two signals is taken. Thus profiles of the backscatter coefficient determined with the Raman method are obtained with high accuracy, i.e., statistical errors of <5–10% and systematic errors of <0.0001 $km^{-1}sr^{-1}$, even at distances of 100 m or less from the lidar.

#### 2.1.5.3. Backscatter Coefficients (Klett Method)

[25] Backscatter coefficients at wavelengths, for which no corresponding molecular signals are measured, have to be evaluated with the so-called Klett method [*Fernald*, 1984]. This method requires two critical input parameters, a reference value of the backscatter coefficient as in the Raman method and a range-dependent ratio of extinction to backscattering, the so-called lidar ratio. The two input parameters influence the solutions for backscatter coefficients below and above ~550 nm in different ways. For the shorter wavelengths the most critical input parameter is the lidar ratio, because it serves to correct the backscatter signals for particle optical depth, which has a higher influence on lidar signals at shorter wavelength. However, in our case, independent information on extinction and backscattering, and thus on the lidar ratio, was typically available at 355 and 532 nm, and occasionally at 292 nm, so that a good estimate for this parameter is always given. The reference value is of minor importance for the short wavelengths and is set, as in the Raman method, into a region with low particle load.

[26] Because of weak Rayleigh scattering, the clear-air assumption for the reference value does not apply for the longer wavelengths. Here the reference height should be located inside a layer of appropriate particle scattering. The Raman solutions for the backscatter coefficient at 355 and 532 nm serve to identify such regions. The reference value is found by taking the short-wavelength results and by extrapolating these under the assumption of a certain wavelength dependence. Optimum for the calibration at the long wavelengths is given, if the reference height can be set into a cirrus layer, as particle backscattering is neutral in this case and short-wavelength values in the cirrus can directly serve as reference values for the long wavelengths. The lidar ratio determined at 532 nm is usually taken as input parameter for the Klett solutions at the longer wavelengths. Because the atmospheric transmission effect on the lidar signals is small, an error in the lidar-ratio estimate is not crucial here.

[27] Additional information for the evaluation of the lidar profiles is provided by independent optical-depth measurements. During LACE 98, Sun and star photometer measurements were taken whenever possible, i.e., in all situations, in which either the Sun or appropriate stars were not covered by

water or ice clouds. A comprehensive data set of the spectral particle optical depth for both daytime and nighttime was thus available [*Ansmann et al*., 2002], and it was possible to compare integrated extinction profiles and integrated backscatter profiles (multiplied by the mean lidar ratio) with these values. In this way, it was independently checked, whether the input parameters for the Klett method were appropriately chosen.

[28] The statistical error of particle backscatter coefficients determined from elastic backscatter signals with the Klett method is <5% for the temporal and spatial resolution used here. Even though the Klett method suffers from its critical input parameters, and systematic errors of the order of 100% must be expected from conventional data analysis, a careful evaluation of the elastic backscatter profiles under consideration of all information, that is available from the combined measurement of elastic and inelastic backscatter profiles and of optical depths at different wavelengths, can reduce the systematic errors to 10–20%.

#### 2.1.5.4. Data Quality Control

[29] In order to invert particle microphysical properties, the optical data from the lidar measurements must be known with an accuracy of better than 10–20% [*Müller et al*., 1999b]. These limits are reached with the careful data evaluation described above. In our case, in addition, special emphasis had to be put on the fact that data from different systems do not deviate in a systematic manner from each other, what might be caused by system or data-evaluation differences. Therefore, several intercomparisons of lidar-derived parameters were performed during LACE 98.

[30] Measurements of profiles at the same or nearly the same wavelength with different systems located next to each other allowed a direct comparison of the derived parameters. This was the case, e.g., for extinction and backscatter coefficients determined with the IfT multiwavelength lidar at 355 nm and the MPI UV lidar at 351 nm or with the IfT multiwavelength lidar and the airborne HSRL at 532 nm. In section 4 a few of these comparisons are presented. The consistency of the data evaluation schemes was proven by the use of synthetic lidar data within the framework of the German Aerosol Lidar Network, part of which the IfT and the MPI lidars are. LACE 98 also served as an instrument intercomparison campaign for this network. An extended discussion of the lidar quality-assurance efforts is given by *Bösenberg et al*. [2001]. In general, we did not observe any systematic deviations in the derived profiles.

### 2.2. Airborne in Situ Instrumentation

[31] The lidar-derived optical and microphysical data were compared with airborne in situ measurements taken aboard two aircraft, a Falcon operated by DLR and a Partenavia operated by IfT and *enviscope* GmbH. These two research aircraft carried a similar payload of aerosol sensing instruments to determine size distribution, scattering and absorption coefficients, and chemical composition of particles in the entire troposphere. Optical particle counters, i.e., condensation nucleus counters (CNC), passive cavity aerosol spectrometer probes (PCASP), and forward scattering spectrometer probes (FSSP) were used to discriminate and count particles with radii from 1.5 nm to 10 $\mu$m. Integrating nephelometers and particle soot absorption photometers (PSAP) measured the particle scattering and absorption coefficients, respectively. Filter samples were taken for a subsequent analysis of particle size, morphology, and elemental composition. Except for the FSSP-300 of the Falcon, which was mounted in a wing station and measured the particles in their ambient state, all airborne instruments sensed the aerosol in its dry state behind a particle inlet. A humidity-growth correction can be applied to the Falcon measurements by comparing the PCASP and the FSSP-300 results in their size overlap region (particle radius from 0.15 to 1.5 $\mu$m). For measurements in the boundary layer the size distributions derived from this correction procedure showed good agreement with those obtained by applying standard growth factors for ammonium-sulfate particles reported by *Tang and Munkelwitz* [1994], which in turn agree well with the findings from hygroscopicity measurements at ground during LACE 98 [*Busch et al*., 2002]. The standard growth factors were thus used to convert the Partenavia measurements to ambient conditions. An overview of the aircraft equipment is given by *Ansmann et al*. [2002]. Principles and data evaluation are described by *Fiebig et al*. [2002], *Petzold et al*. [2002], and *Wendisch et al*. [2002].

[32] The fast-flying ($\geq$120 m s$^{-1}$) Falcon usually descended from the tropopause to the lower boundary layer in several U-shaped flight legs of approximately 60-km length in north-south direction close to Lindenberg. The slow-flying (60–70 m s$^{-1}$) Partenavia with a ceiling of 4 km scanned the boundary layer and the lower free troposphere during slow ascents and descents above the LACE field site. Details on flight strategy and flight patterns are discussed by *Petzold et al*. [2002].

## 3. Inversion Methods

### 3.1. Inversion Problem

[33] Two inversion algorithms developed at the IfT and at the IMP are used to derive microphysical particle properties from the multiwavelength lidar measurements. In the inversion, a set of equations, which relate the optical data to the underlying physical quantities, has to be solved numerically:

$$g_i(\lambda) = \int_0^\infty K_i(r,m,\lambda,s)\frac{3}{4r}v(r)dr\,, \quad g_i = \alpha,\beta\,, \qquad (1)$$

where $g_i(\lambda)$ denotes the extinction coefficient $\alpha$ or the backscatter coefficient $\beta$ at wavelength $\lambda$, $v(r)$ describes the volume concentration of particles per radius interval d$r$, and $K_i(r, m, \lambda, s)$ is the kernel efficiency of extinction or backscattering for single particles. The efficiencies depend on the radius $r$ of the particles, on their complex refractive index $m$, on the wavelength $\lambda$ of the interacting light, and on the shape $s$ of the particles. They are calculated from Mie-scattering theory under the assumption that small particles in a first approximation behave like spherical scatterers [*Bohren and Huffman*, 1983].

[34] Equation (1) represents a system of Fredholm integral equations of the first kind, which has to be solved in a numerical fashion. The determination of the particle volume distribution $v(r)$ and the complex refractive index from a small number of measured backscatter and extinction coefficients with this equation system is a nonlinear, inverse, ill-posed problem, i.e., solutions are nonunique and highly oscillating without the introduction of appropriate mathematical tools such as discretization and regularization. In other words, this approach can be described as an eigenvalue analysis of the system of integral equations.

### 3.2. IfT Algorithm

[35] The IfT scheme, which is described in detail by *Müller et al*. [1999a], uses a Tikhonov regularization with constraints. It has been specifically designed for the inversion of the eight optical data measured with the IfT multiwavelength lidar (backscatter coefficients at 355, 400, 532, 710, 800, 1064 nm and extinction coefficients at 355, 532 nm). The volume concentration distribution, which has to be determined from equation (1), is approximated with a discrete set of eight weighted base functions, which are B splines of the first order, i.e., they have a triangular shape on a semilogarithmic scale. The shape of the investigated particle size distribution does not have to be known a priori. The numerical solution of equation (1) provides the sought weight factors. In the solution process, the constraint of smoothness of the retrieved volume concentration distribution serves as the regularization parameter for the stabilization of the inverse problem. The degree of this regularization, which acts as a trade-off against the ability to reproduce the input optical data with the found inversion solutions, is determined with generalized cross-validation [*Golub et al*., 1979]. Fifty inversion windows of variable width are defined through variation of the lower and upper limits of the base-function range from 0.01 to 0.2 and from 1 to 10 $\mu$m, respectively. The base functions are distributed logarithmically equidistant within the windows. The inversion is performed for every window and for a grid of wavelength- and size-independent complex refractive indices that vary from 1.33 to 1.8 in real and from 0 to 0.7 in imaginary part.

[36] In the final step, from the individual inversion solutions only those are selected, for which the back-calculated optical data agree with the original data within the limits of the measurement error. The mean particle size in terms of the effective radius and integral particle parameters, i.e., the total volume, surface-area, and number concentrations, are calculated from the selected solutions, and their mean values and standard deviations are presented as final inversion results. In this way, one also obtains a range of complex refractive indices. The single-scattering albedo is then calculated from the volume concentration distribution and the mean complex refractive index.

[37] From extended simulation studies, it was shown that an appropriate reconstruction of the volume distribution together with a mean complex refractive index is found from the eight optical data derived with the IfT multiwavelength lidar [*Müller et al*., 1999b]. It was demonstrated that information on particle extinction is necessary at two wavelengths at least and that the optical data must be determined with errors of $\leq$10–20%.

### 3.3. IMP Algorithm

[38] The hybrid regularization technique developed at IMP is designed to work with different kind and number of optical data, i.e., experimental data obtained with different systems at various wavelengths can be evaluated [*Böckmann and Sarközi*, 1999; *Böckmann*, 2001]. In the first case presented below, backscatter coefficients at 320 and 728 nm and extinction coefficients at 292 nm were used in addition to the eight data of the IfT lidar. In the second case, backscatter and extinction coefficients at 351 nm were added to the data set of the IfT lidar.

[39] Similar to the IfT scheme, the algorithm does neither require any a priori information on the analytical shape of the investigated distribution function nor an initial guess of it. Multimodal distributions can be retrieved without any knowledge of the number of modes in advance.

[40] The first regularization step in this method is performed via discretization, in which the investigated distribution function is approximated with B spline functions of different order, which implies different shapes of these functions. The projection dimension, i.e., the number of base functions serves as another regularization parameter. In the second step, regularization is controlled by the level of truncated singular-value (or eigenvalue) decomposition performed during the solution process of the resulting linear equation system. In this way, eigenvalues and corresponding eigenvectors, which lead to oscillating solutions, are omitted. In order to reduce the computer time, a collocation projection is used.

[41] As in the case of the IfT scheme, the highly nonlinear problem of the complex refractive index as a second unknown is handled by introducing a grid of wavelength- and size-independent mean complex refractive indices and by enclosing the area of possible real/imaginary-part combinations through inversion and back-calculation of optical data. Again, inversion results are given in terms of effective particle radius, volume, surface-area, and number concentrations.

## 4. Case Studies

[42] Two measurement cases with very different aerosol characteristics were chosen for the studies presented here. On 9 and 10 August 1998 a long-range transported, biomass-burning aerosol, that had originated from forest fires in northwestern Canada, was observed between ~3- and 6-km height in an air mass, that was almost not influenced by other pollution. A relatively low particle optical depth of 0.1–0.15 at 550 nm was found. A unique observational situation occured in the night of 9 to 10 August, when the Falcon was on a nighttime mission and all lidar systems described in subsection 2.1 made simultaneous measurements. Particle backscatter coefficients at eight wavelengths and particle extinction coefficients at three wavelengths could be determined and used in the inversion. The inversion results could be directly compared to the in situ data, because the relative humidity in the aerosol layer was low, so that it was not necessary to apply a humidity-growth correction to the aircraft data.

[43] On 11 August 1998, polluted air was advected in the planetary boundary layer to the measurement site from different industrial regions in Europe. Particle optical depths of ~0.35 at 550 nm were measured on that day. Particle backscatter coefficients at seven wavelengths and particle extinction coefficients at three wavelengths were measured with two ground-based lidars in the evening. The inversion results are compared to parameters measured in situ aboard the Partenavia at daytime.

### 4.1. Biomass-Burning Aerosol From Canada

#### 4.1.1. Measurement Situation

[44] A distinct aerosol layer in the free troposphere was observed at the LACE 98 field site from the morning of 9 August to the evening of 10 August 1998. During daytime, faint, wave-like structures could be seen by eye. Routine weather observers in northern Germany reported cirrus overcast. However, only a few cirrus cloud fields were detected with lidar on 9 August, and the atmosphere was absolutely cloud-free on 10 August [*Ansmann et al*., 2002].

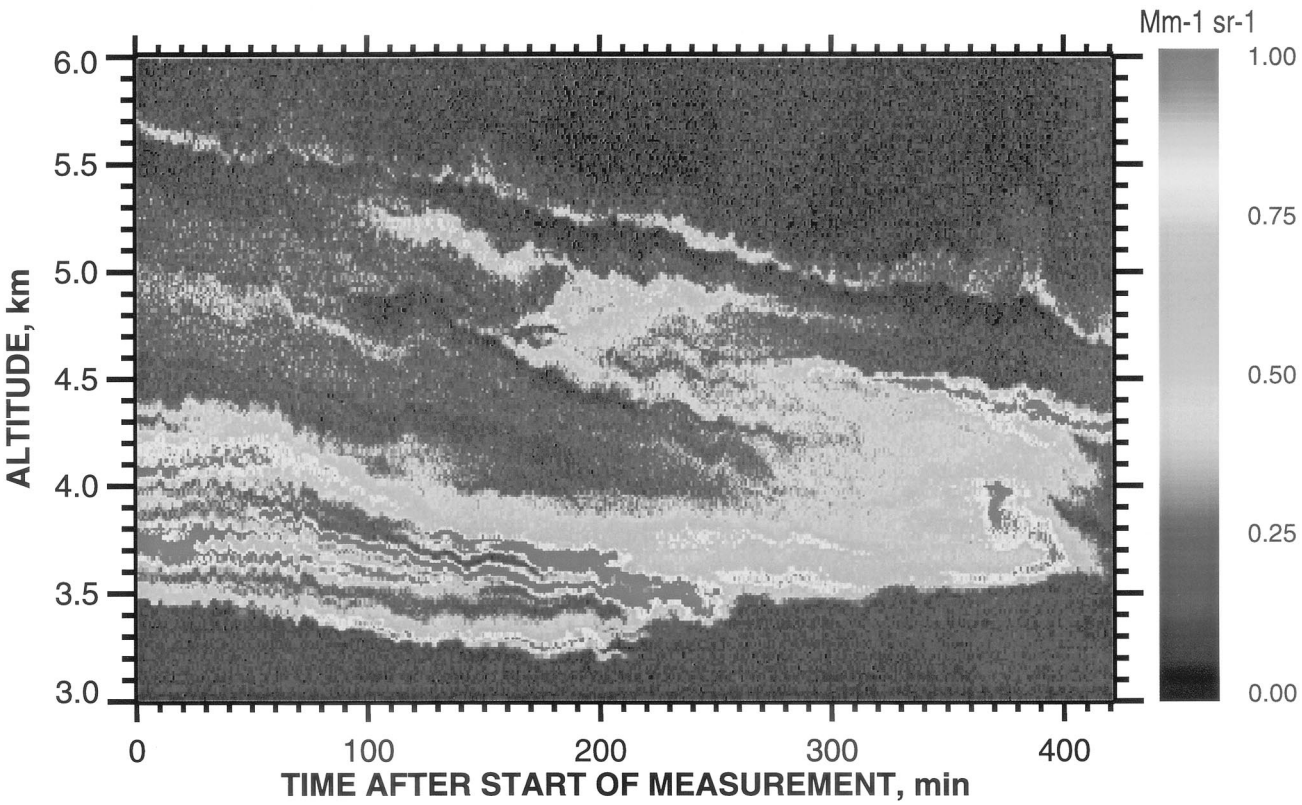


**Figure 1.** Backscatter coefficient at 532 nm in the biomass-burning aerosol layer from 2000 UTC on 9 August to 0300 UTC on 10 August 1998. The measurement was taken with the IfT multiwavelength lidar. The resolution is 15 m in height and 30 s in time. See color version at back of this issue.

[45] Figure 1 shows the development of the elevated aerosol layer in terms of the particle backscatter coefficient at 532 nm on a time-height scale, based on the observations with the IfT multiwavelength lidar between 2000 UTC on 9 August and 0300 UTC on 10 August. The lidar provides a detailed view into the complex aerosol fine structure and shows well-separated single layers of a few tens of meters in vertical extent, gravity waves, and turbulences. The backscatter maximum for this night was observed between 3.4- and 3.8-km height from about 2200 to 2400 UTC (see Figure 1, minutes 120 to 240). During that time also the Falcon flight was carried out. Consequently, this time interval was chosen for further investigation.

[46] Figure 2 gives an overview of the situation in the entire troposphere from 2200–2400 UTC on 9 August. The backscatter-coefficient profiles in Figure 2a are determined after the Raman method at 532 nm with a height resolution of 180 m. They are calibrated to 0.0001 $km^{-1}sr^{-1}$ in the height region from 6100–6800 m. This value corresponds to the one obtained for this height region from the particle size distribution measured in situ aboard the Falcon and under the assumption of a refractive index of $1.53–10^{-7}i$ [*Fiebig et al.*, 2002]. The 2-hour average of the backscatter-coefficient profile is shown together with the four respective 30-min means (see Figure 2). The profiles indicate stable aerosol conditions below 3 km. The free-troposphere aerosol layer showed a quite stable, pronounced maximum around 3.75 km. The second maximum observed between 4.5 and 5 km was more variable. Different cirrus cloud fields were present in two layers, from 7.5- to 10- and from 10.5- to 12.5-km height.

[47] The relative humidity determined with the IfT multiwavelength lidar between 2200 and 2400 UTC and with a radiosonde launched at 2254 UTC from the field site is shown in Figure 2b. The lidar-derived relative humidity is calculated from the water-vapor mixing ratio obtained with the Raman method and a radiosonde temperature profile. The lidar measurements of water vapor could not be extended into the cirrus clouds because of low signal-to-noise ratios. Quite dry conditions with relative-humidity values of $<40\%$ were found in the main part of the free-troposphere aerosol layer. At the upper boundary of the layer around 5.5-km height, values up to 60% were measured. The potential and equivalent potential temperatures, which are also given in Figure 2b, indicate a stable layering of the atmosphere.

[48] In Figure 3, eight-day backward trajectories arriving at Lindenberg at 2300 UTC are presented. These long-term three-dimensional backward trajectories were calculated with the flexible trajectory model FLEXTRA (version 3.2d) [*Stohl et al.*, 1995]. FLEXTRA was driven with hemispheric model-level wind fields provided by the European Centre for Medium-Range Weather Forecasts (T213 L31 model [*ECMWF*, 1995]), with a horizontal resolution of 1° and a time resolution of 3 hours (analyses at 0, 6, 12, 18 UTC; 3-hour forecasts at 3, 9, 15, 21 UTC).

[49] The backward trajectories indicate the advection of air masses throughout the troposphere from the North Atlantic across the North Sea directly to the measurement site. On this way, the air did not cross highly industrialized regions. The backward trajectories for the height region from 3 to 5 km (pressure levels 700–550 hPa) originate from northwestern

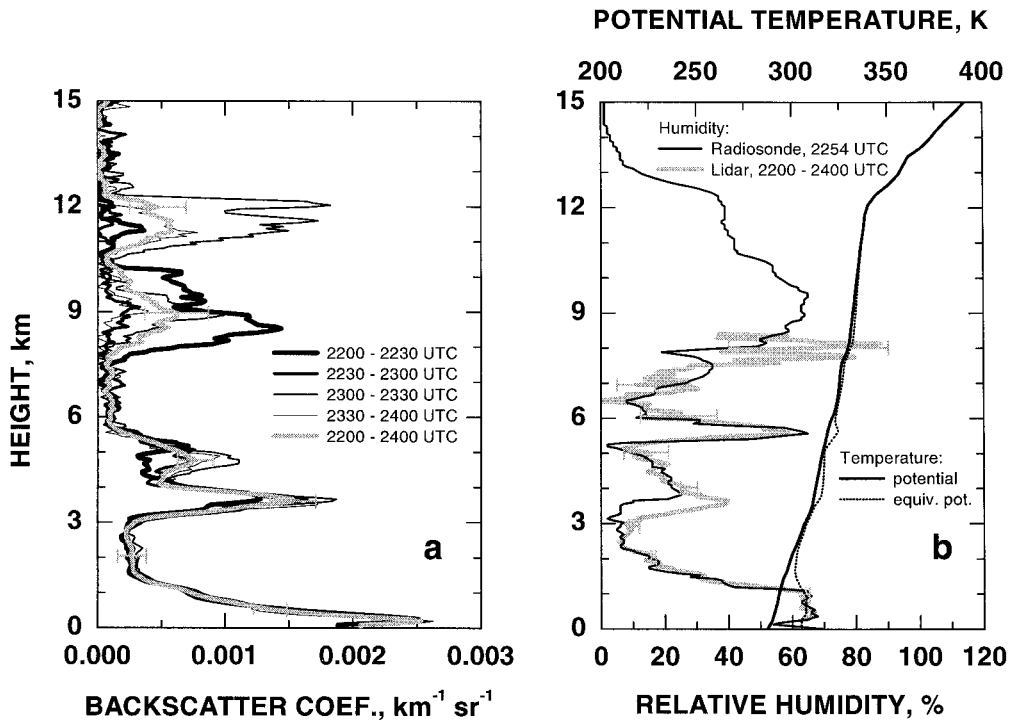


**Figure 2.** Measurement situation on 9 August 1998, 2200–2400 UTC. (a) Particle backscatter coefficient at 532 nm determined after the Raman method with a height resolution of 180 m. The error bars indicate statistical (signal noise) and systematic errors (reference-value estimate). (b) Relative humidity determined with radiosonde and lidar and potential and equivalent potential temperature determined with radiosonde. Height resolution of the lidar measurement is 110 m (0–2000 m), 280 m (2000–4000 m), 560 m (4000–6000 m), and 840 m (above 6000 m). The error bars indicate statistical noise.

Canada. There strong forest fires occured in late July and early August 1998. The gray-shaded areas in Figure 3 indicate the locations of the strongest fires, that burned about 6–10 days prior to the measurement. The trajectory analysis shows that the air mass traveled below 2000-m height in the forest-fire region and was then lifted above southern Greenland. An additional mixing of polluted and clean air masses might have occurred there around 450 hPa. Almost all air parcels with arrival heights of 2–6 km crossed southern Greenland in this height level 40–80 hours prior to the measurement. The remarkable event of the transport of forest-fire aerosols from northwestern Canada to Europe was also observed with satellites [*Hsu et al.*, 1999]. A detailed analysis of the transport of the fire emissions to Europe in August 1998 is presented in a separate paper [*Forster et al.*, 2001].

#### 4.1.2. Spectral Backscatter and Extinction Coefficients

[50] Backscatter-coefficient and extinction-coefficient profiles in the forest-fire aerosol layer at all available wavelengths are shown in Figure 4. Eight backscatter coefficients in the wavelength region from 320–1064 nm and three extinction coefficients at 292, 355, and 532 nm were determined from measurements with the IfT multiwavelength lidar, the MPI UV lidar (operated with KrF), and the MPI water-vapor DIAL (see section 2). The backscatter coefficients at 355 and at 532 nm were calculated with the Raman method, whereas the Klett method was applied to the elastic backscatter signals at all other wavelengths. Lidar ratios of the biomass-burning aerosol layer were found to be between 40 and 80 sr at 532 nm (see below). For the Klett method, a lidar ratio of 50 sr was used at all wavelengths. Because of the low optical depth of the aerosol layer of the order of 0.1, the lidar-ratio estimate is less critical here. To estimate the reference values, the airborne in situ measurements in the height region from 6100–6800 m were used as mentioned above. These results were checked against those obtained by assuming wavelength-independent backscattering in the two cirrus layers at 9- and 11.5-km height (see Figure 2). That is, the reference values used in the Klett method were taken from the 532-nm backscatter profile calculated with the Raman method within the cirrus. The profiles calibrated in the cirrus cloud deviated by $<10\%$ from the profiles calibrated between 6100- and 6800-m height with the help of the airborne in situ measurements.

[51] A comparison of an airborne HSRL measurement with a ground-based Raman measurement at 532 nm is shown in Figure 5. The airborne profiles were derived from a 100-s measurement taken on a 15-km leg $\sim$5 km to the east of Lindenberg at 2240 UTC. The backscatter-coefficient, extinction-coefficient, and lidar-ratio profiles determined with the two different systems agree very well within the limits of the measurement uncertainties. Deviations between the profiles are mainly caused by spatial and temporal variations in the aerosol layer (see also Figure 2a). An inspection of the time-height contour plots for the ground-based (see Figure 1) and airborne measurements [see *Fiebig et al.*, 2002, Figure 1b] indicates that very similar structures in the aerosol layer were observed with both systems. As the aerosol layer moved from northwest to southeast, the airplane sensed the air mass, that had moved across the Lindenberg area the hour before. As can be seen from Figure 5, a slightly better agreement of the

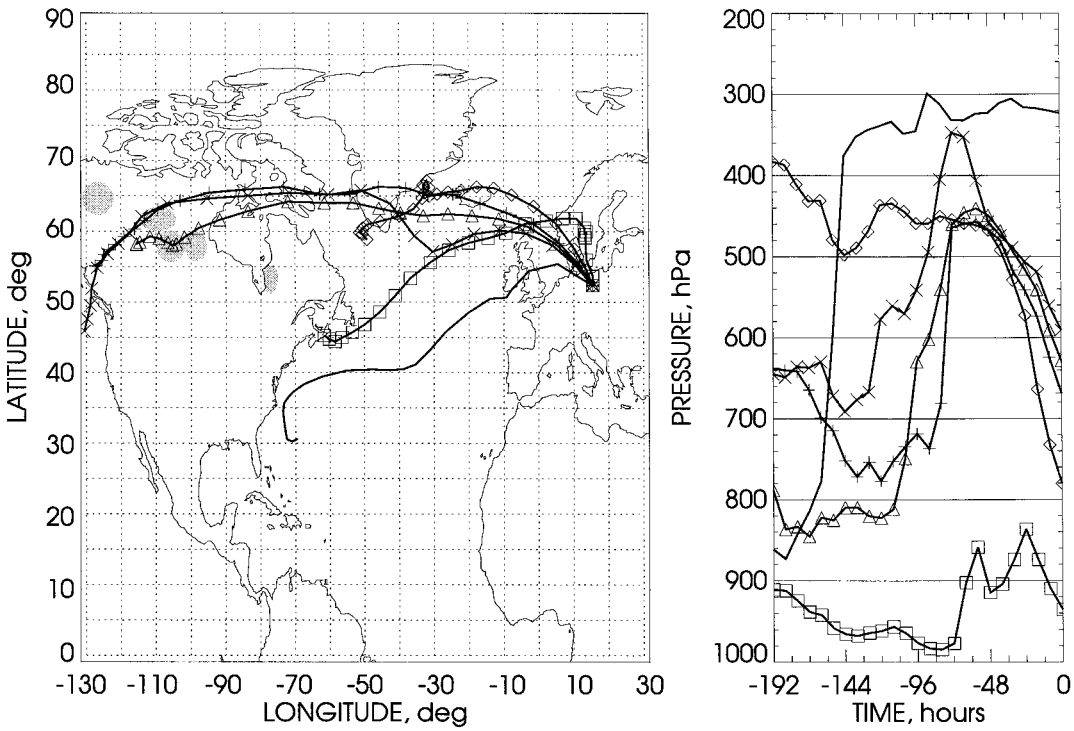


**Figure 3.** Eight-day backward trajectories with arrival at Lindenberg on 9 August 1998, 2300 UTC. The arrival heights above Lindenberg are 645, 2145, 3395, 3895, 4395, and 8895 m (right panel, time 0, from bottom to top). The left panel presents a horizontal projection of the trajectories with their positions marked every 8 hours. Gray-shaded areas indicate the locations of forest fires in Canada around 1–4 August 1998.

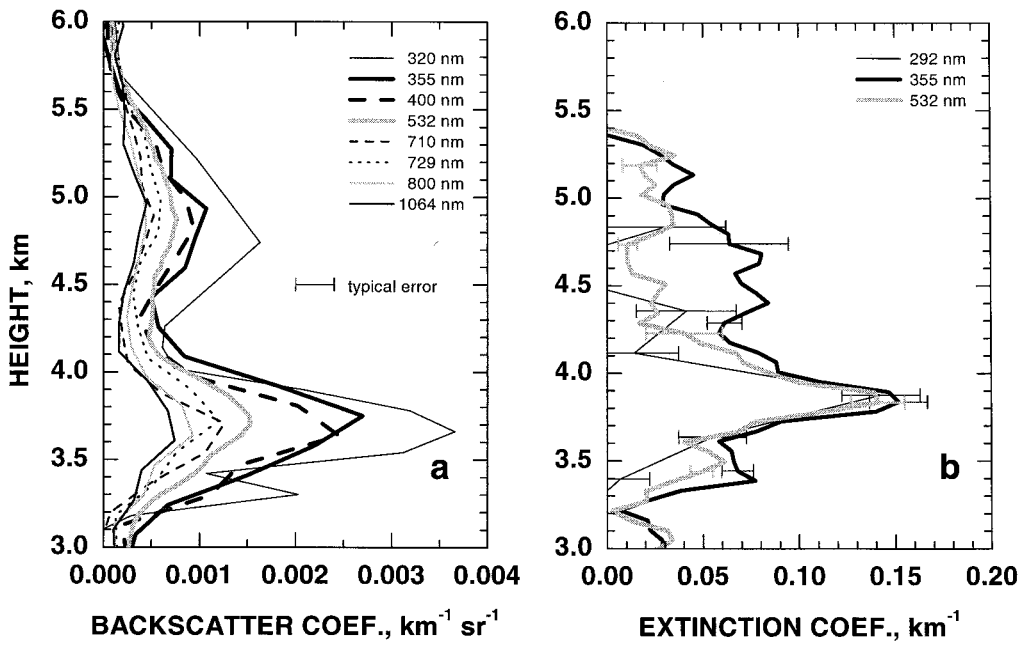


**Figure 4.** (a) Backscatter coefficients and (b) extinction coefficients measured in the biomass-burning free-troposphere aerosol layer at Lindenberg on 9 August 1998, between 2200 and 2400 UTC. The height resolution is 120 m (320 nm), 165 m (355, 400, 532, 710, 800, 1064 nm), and 180 m (729 m) for the backscatter coefficients and 240 m (289 nm), 390 m (355, 532 nm, below 3840 m), and 780 m (355, 532 nm, above 3840 m) for the extinction coefficients. The error bars are dominated by systematic errors in the case of backscattering and by statistical errors in the case of extinction.

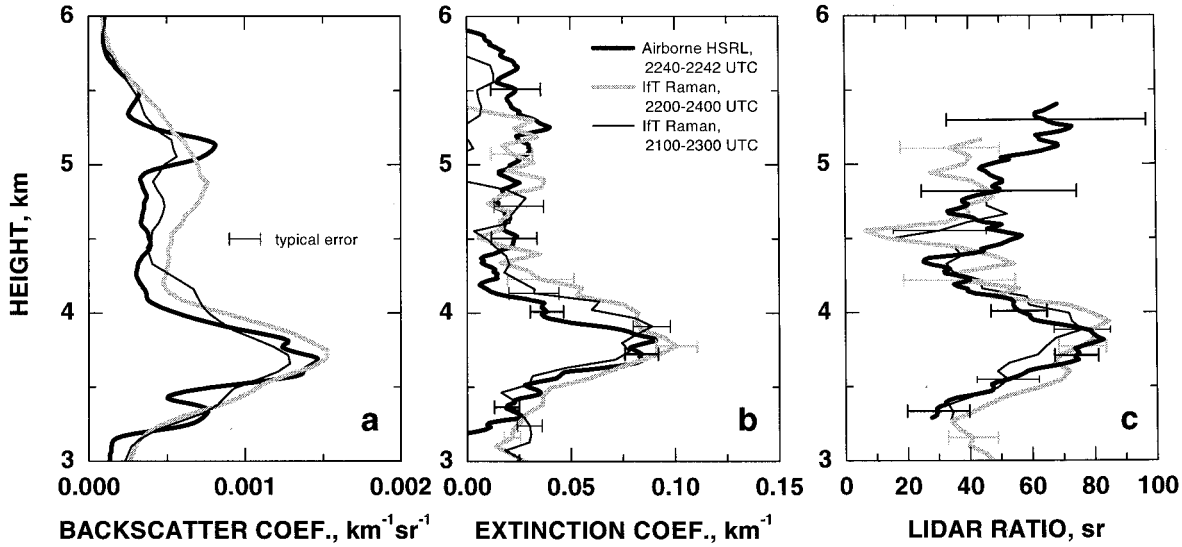


**Figure 5.** (a) Backscatter coefficients, (b) extinction coefficients, and (c) lidar ratios at 532 nm measured in the biomass-burning free-troposphere aerosol layer with the IfT multiwavelength lidar at Lindenberg on 9 August 1998, 2100–2300 and 2200–2400 UTC, and with the airborne HSRL near Lindenberg on 9 August 1998, 2240–2242 UTC. The height resolution for the ground-based system is 165 m for the backscatter coefficient, 560 and 840 m for the extinction coefficient below and above 4180 m, respectively, and 840 m for the lidar ratio. The height resolution for the airborne system is 180 m for the backscatter coefficient, 600 m for the extinction coefficient and 900 m for the lidar ratio. The error bars indicate systematic and statistical errors in the case of backscattering and the statistical error in the case of extinction and lidar ratio.

profiles is found, if one takes an average from 2100–2300 UTC instead from 2200–2400 UTC for the ground-based measurements.

[52] In Figure 6 the spectral backscatter and extinction coefficients for two height regions of the aerosol layer are plotted. The values are taken from the profiles shown in Figure 4. An additional averaging was applied in order to reduce the statistical error and to obtain the same height resolution for extinction and backscatter coefficients. The height intervals from 3500–4000 m and from 4200–5400 m represent two regions of the aerosol layer with obviously different particle microphysical properties. In the main peak of the layer around 3750-m height, wavelength-independent extinction and a rather steep spectral slope of backscattering was observed, whereas in the upper part of the layer the extinction in the UV was higher than in the visible and the wavelength dependence of backscattering was weaker. Similar spectra as shown in Figure 6 were found for other averaging intervals within the two height ranges below and above 4000 m.

[53] Extinction and backscatter coefficients at the lidar wavelengths were also calculated from the particle size distribution measured in situ [see *Fiebig et al.*, 2002, Figures 3 and

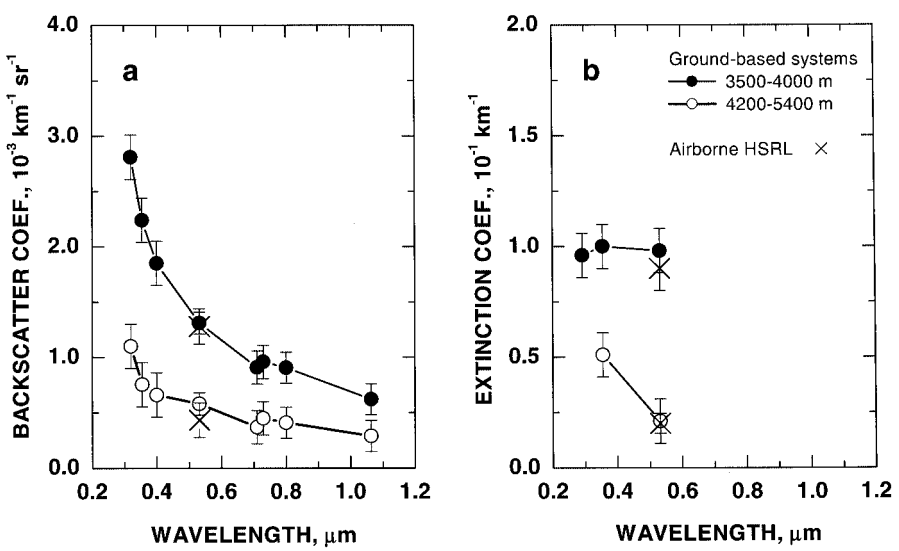


**Figure 6.** (a) Spectral backscatter coefficients and (b) spectral extinction coefficients for the height regions 3500–4000 and 4200–5400 m as derived from the profiles shown in Figures 4 and 5. The error bars indicate statistical and systematic uncertainties.

**Table 1.** Physical Particle Parameters From Inversion of Lidar Data Measured in the Height Region From 3500–4000 m on 9 August 1998, 2200–2400 UTC, and From in Situ Measurements of Particle Size Distributions Aboard the Falcon From 3400–3900 m

| | Lidar, Inversion | | Falcon, in Situ | |
|---|---|---|---|---|
| Parameter | IfT Algorithm | IMP Algorithm | Particles With $r \geq 1.5$ nm | Particles With $r \geq 50$ nm |
| $r_{\text{eff}}$,[a] $\mu$m | 0.27±0.04 | 0.24±0.01 | 0.24±0.06 | 0.25±0.07 |
| $v_t$,[b] $\mu m^3 cm^{-3}$ | 13±2 | 11±1 | 9±5 | 8±5 |
| $a_t$,[c] $\mu m^2 cm^{-3}$ | 139±7 | 136±5 | 110±50 | 95±55 |
| $n_t$,[d] $cm^{-3}$ | 291±70 | 506±131 | 640±174 | 271±74 |
| $m_{\text{real}}$[e] | 1.64±0.09 | 1.66±0.02 | (1.56) | (1.56) |
| $m_{\text{imag}}$[f] | 0.05±0.02 | 0.053±0.004 | (0.07) | (0.07) |
| SSA[g] (532 nm) | 0.83±0.06 | 0.79±0.01 | 0.78±0.02 | 0.79±0.02 |

[a]Here $r_{\text{eff}}$, effective radius.
[b]Here $v_t$, total volume concentration.
[c]Here $a_t$, total surface-area concentration.
[d]Here $n_t$, total number concentration.
[e]Here $m_{\text{real}}$, real part of refractive index.
[f]Here $m_{\text{imag}}$, imaginary part of refractive index.
[g]SSA, single-scattering albedo.

8]. The refractive index was estimated by assuming a mixture of absorbing, soot-like and nonabsorbing, ammonium-sulfate-like material. Internal and external mixtures of these components were considered, and the soot content was chosen such that the calculated absorption coefficient agreed with the one measured with the PSAP. The spectral slope of the calculated extinction coefficient was not sensitive to the state of mixture, and the calculated values agreed well with the lidar data. In contrast, the spectral slope of the backscatter coefficient measured with lidar could only be reproduced with the calculations for an external mixture. Calculated backscatter coefficients in the UV for an internal mixture were a factor of 3–4 smaller than those for an external mixture and the measured ones. The calculations were also performed for iron oxide as an absorbing material, since both carbon and iron oxide were obtained in the chemical analysis of filter probes taken in the aerosol layer. However, the lidar data could only be reproduced if less than 5% of the particle volume were attributed to iron oxide. The steep increase in the imaginary part of the refractive index of iron oxide around 550 nm leads to an increase of the calculated backscatter spectrum between 500 and 800 nm, which is not consistent with the measurement [see *Fiebig et al*., 2002, Figure 8]. From the comparison of measured and calculated backscatter coefficients it was thus concluded that the aerosol in the biomass-burning layer consisted of an external mixture of nonabsorbing ammonium-sulfate-like material, a fraction of 30–35% soot, and less than 5% iron oxide.

#### 4.1.3. Inversion Results

[54] The optical data shown in Figure 6 were used as input in the two inversion algorithms described in section 3. The IfT algorithm uses the six backscatter and two extinction coefficients of the IfT multiwavelength lidar, whereas in the IMP algorithm different numbers and combinations of data can be processed. Therefore several tests were performed with the IMP scheme to check the influence of certain wavelengths on the inversion results.

[55] Tables 1 and 2 show the inversion results for the two chosen height ranges of the biomass-burning aerosol layer in comparison to the Falcon in situ measurements. Because the humidity was well below 50% in the investigated height regions and no significant difference in the overlap region of the size distributions measured with PCASP and FSSP on board the Falcon was found [see *Fiebig et al*., 2002, Figure 3] the airborne data were not corrected for humidity growth. The hygroscopicity of smoke particles tends to be smaller than the one of other pollution aerosols, and significant changes of particle scattering properties and size are observed for humidities >50% only [*Kotchenruther and Hobbs*, 1998].

[56] The size parameters in Tables 1 and 2 agree well within their error limits. This holds for the comparison between the two inversion algorithms as well as for the comparison between inversion results and in situ data. On average, the three methods gave an effective radius of 0.25±0.03 $\mu$m for the

**Table 2.** Same as Table 1, but for Lidar Measurements From 4200–5400 m and in Situ Measurements From 4400–5000 m

| | Lidar, Inversion | | Falcon, in Situ | |
|---|---|---|---|---|
| Parameter | IfT Algorithm | IMP Algorithm | Particles With $r \geq 1.5$ nm | Particles With $r \geq 50$ nm |
| $r_{\text{eff}}$, $\mu$m | 0.23±0.02 | 0.16±0.01 | 0.17±0.04 | 0.18±0.05 |
| $v_t$, $\mu m^3 cm^{-3}$ | 3.4±0.4 | 2.3±0.2 | 6±3 | 6±3 |
| $a_t$, $\mu m^2 cm^{-3}$ | 44±1 | 44±3 | 100±45 | 91±53 |
| $n_t$, $cm^{-3}$ | 663±224 | 937±316 | 754±174 | 354±74 |
| $m_{\text{real}}$ | 1.76±0.05 | 1.77±0.02 | - | - |
| $m_{\text{imag}}$ | 0.046±0.005 | 0.043±0.01 | - | - |
| SSA (532 nm) | 0.78±0.01 | 0.83±0.04 | - | - |

lower part of the biomass-burning aerosol layer, whereas the particles in the upper part of the layer were slightly smaller in size with an effective radius of $0.19 \pm 0.02$ $\mu$m. Surface-area and volume concentrations derived from the inversions are about 30% higher than those measured in situ in the lower layer, whereas in the upper layer the values measured in situ are 50–60% higher than the inverted data. This deviation can be attributed to the spatial inhomogeneity of the aerosol layer rather than to uncertainties in either the measurement or the inversion. Approximately the same differences are found from the comparison of the absolute backscatter and extinction coefficients measured with lidar and those calculated from the in situ measured size distribution. The relative spectral slope of extinction and backscatter coefficients, however, is the same. In a first approximation the particle volume concentration is proportional to the backscatter coefficient and the particle surface-area concentration is proportional to the extinction coefficient. Changes in the absolute values of the optical data as shown in Figure 1 and Figure 2a thus indicate changes in the particle concentration as long as the same aerosol type is observed.

[57] Number concentrations are difficult to determine from the inversion of optical data [*Müller et al*., 1999b] because usually the majority of particles is too small to be optically active and thus does not contribute to the optical coefficients measured with lidar. If one separates the in situ measurements into the different modes of the size distribution (Aitken mode with particle radii $r<0.05$ $\mu$m, accumulation mode with $0.05<r<0.5$ $\mu$m, and coarse mode with $r>0.5$ $\mu$m), it becomes evident that in the present case more than 50% of the particles belonged to the Aitken mode. The inversion of the multiwavelength lidar data, however, gives mainly information on particles in the accumulation and coarse modes. Because the Aitken mode does not significantly contribute to total particle surface area and volume, these concentrations, and thus also the effective radius, are reconstructed very well with the inversion. The uncertainty in the derivation of the number concentration is indicated by the large error limits, which are obtained from the scattering of the respective parameter within the solution space. An error of more than about 25% normally indicates a failure in the determination of the number concentration. Simulations furthermore revealed that in such cases a considerable systematic shift toward higher or lower number concentrations may occur.

[58] The inversion results for the lower part of the layer show the real part of the refractive index at about 1.65. In the upper part of the layer, even higher values around 1.76 were obtained. Imaginary parts of about 0.05 and 0.045 were found for the lower and upper parts of the layer, respectively. As mentioned in section 3, a variable, but wavelength- and size-independent mean complex refractive index is used in both inversion schemes. As has been shown previously [*Müller et al*., 1999b, 2000a; *Böckmann*, 2001], solutions are obtained for certain combinations of real and imaginary parts of the complex refractive index only. If the real and imaginary parts are ordered in a matrix-like scheme, the solutions for the refractive index are arranged along a diagonal in this matrix. That is, smaller real parts are connected with smaller imaginary parts and larger real parts with larger imaginary parts. This fact should be taken into account in the interpretation of the error limits given for the refractive index.

[59] The refractive index for the airborne in situ measurements was calculated from a volume-weighted, internal mixture of absorbing, soot-like and nonabsorbing, ammonium-sulfate-like material under consideration of the absorption coefficient measured with the PSAP. This was done for the lower layer only, because no reliable absorption measurements were available in the upper height region. One should have in mind that closure of the backscatter coefficients calculated from the size distribution with the lidar backscatter coefficients was obtained for an external mixture of the two aerosol components only, i.e., by introducing a separate refractive index for ammonium sulfate of $1.53-0.0i$ and for soot of $1.75-0.45i$ [*Fiebig et al*., 2002]. Calculations for an internal mixture could not reproduce the lidar measurements. For that reason, the values in Table 1 are given in parentheses because they are only a very rough estimate.

[60] The values for the single-scattering albedo, which are derived from the particle size distributions and the complex refractive indices with Mie-scattering calculations, are 0.78–0.83. They are in good agreement with the airborne results, which are calculated from the measured size distribution and an external mixture of soot and ammonium sulfate.

[61] The sensitivity studies with the IMP algorithm concerning the different number of data used in the inversion showed that, e.g., the use of six backscatter and two extinction coefficients determined with the IfT multiwavelength lidar instead of all 11 available optical data (eight backscatter and three extinction coefficients) did not change the results for particle size and concentration significantly. However, a remarkable sensitivity of the complex refractive index was noted. Especially, the introduction of the extinction values at the shortest wavelength (292 nm) lead to a very large solution space, which included unrealistically high real and imaginary parts of the refractive index. One possible reason for that is the large uncertainty of the values in the UV because of the necessary ozone correction. On the other hand, refractive indices can remarkably change from visible to UV wavelengths. The approach to use a mean, wavelength-independent refractive index may fail here, because the influence of the wavelength dependence becomes too high.

#### 4.1.4. Discussion

[62] The particles of the biomass-burning aerosol layer with an effective radius of about 0.25 $\mu$m or a count median diameter (CMD) of the accumulation mode of 0.30 $\mu$m [*Fiebig et al*., 2002] were considerably larger than those found in other smoke plumes. *Reid et al*. [1998] reported CMD values of 0.12 $\mu$m for very young particles to 0.21 $\mu$m for particles of an age of a few days near the burning rain forests in Brazil. *Radke et al*. [1988] obtained values of about 0.22 $\mu$m near forest fires in North America and a tendency that particles grow with age. From the transport calculations [*Forster et al*., 2001] it was found that the age of the particles in the biomass-burning aerosol observed at Lindenberg was about six days. During their travel from the American to the European continent the particles reached heights of 6–8 km, before they descended into the measurement area (see Figure 3). Ageing processes such as condensation, coagulation, photochemical transformations, and cloud processing might be responsible for the growth of the particles.

[63] The complex refractive index was found to be higher compared to values previously reported for biomass-burning aerosols. Real parts ranged from 1.5 to 1.6 at visible wavelengths [*Yamasoe et al*., 1998; *Remer et al*., 1998]. Higher real parts were correlated with decreasing relative humidity. For

the imaginary part values of 0.01–0.04 were found [*Anderson et al*., 1996; *Li and Mao*, 1990; *Lenoble*, 1991]. One explanation for our overestimation might be that in the present case highly absorbing iron oxide was found [*Fiebig et al*., 2002]. Although only present in minor concentrations, the respective very high complex refractive index might have led to the observed high values. The considerably low relative humidities of <40% within the layer may have contributed to these values as well.

[64] Values of the single-scattering albedo of the order of 0.8 found in the layer are comparably small and indicate a rather high influence of absorption of the particles. Radiative-transfer calculations for the biomass-burning aerosol are presented by *Fiebig et al*. [2002]. Single-scattering albedos in very young smoke ranged from 0.3 to 0.9 with a mean value of 0.75, whereas aged smoke particles showed single-scattering albedos of 0.80–0.84 in the case of the Brazilian fires [*Reid and Hobbs, 1998; Reid et al*., 1998; *Hobbs et al*., 1997]. *Anderson et al*. [1996] reported values of 0.79 and 0.81 for dry particles in African and Brazilian outflows over the South Atlantic. Higher values of 0.85–0.90 were found for boreal fires [*Radke et al*., 1988].

### 4.2. Continental European Pollution

#### 4.2.1. Measurement Situation

[65] The measurement situation changed significantly from 10 to 11 August 1998. Starting in the night of 10/11 August, heavily polluted air was advected in the boundary layer above Lindenberg. The optical depth at 550 nm increased from values of the order of 0.05 on 10 August to values around 0.35 on 11 August [*Ansmann et al*., 2002]. The lidar measurements presented here were taken after sunset from 2020–2220 UTC on 11 August 1998. No simultaneous flights were performed during that time, and airborne measurements taken between 1200 and 1300 UTC are available for comparison on that day only. Therefore the measurement situation is discussed with respect to the comparability of the two time periods in the following. Because a better resolution of data in the boundary layer is available from the slow-flying aircraft, the Partenavia in situ measurements taken around 1230 UTC were used for all comparisons shown in subsections 4.2.2 and 4.2.3.

[66] Figure 7 shows the trajectory analysis for 1300 and 2100 UTC on 11 August 1998, with focus on the lower troposphere. Again, FLEXTRA simulations were used to obtain information for the airborne and lidar measurement times. From all trajectories, which are available with a height resolution of 250 m, four characteristic levels were chosen for the presentation in Figure 7. The trajectory analysis revealed that two different air masses contributed to the observed pollution. In the lowest heights the air traveled from the North Atlantic, crossed southern Scandinavia and Poland, and reached the measurement site from eastern (near ground) to southern directions (around 1-km height). During this travel the air mass descended from the free troposphere into the boundary layer, where it could be loaded with precursor gases and particles presumably at distances of <300 km from the field site within 24–36 hours before the measurement. At higher altitudes the air reached Lindenberg from the west. For about 3–4 days this air had circled in the boundary layer over industrialized regions in western and central Europe, before it was lifted during the 24 hours prior to the arrival at Lindenberg. The lifting was stronger for the air mass that arrived during the flight mission (1300 UTC, see Figure 7a) than for the air mass that was measured in the evening (2100 UTC, see Figure 7b). This finding of the trajectory analysis is consistent with the lidar observations. A heavy pollution layer was detected between 2- and 3-km height (800–700 hPa, see Figure 7a) around noon. This layer descended during the afternoon and was observed between 1.2- and 2-km height (860–800 hPa, see Figure 7b) in the evening.

[67] Two conclusions can be drawn from the trajectory analysis. First, one can expect two aerosol types of different origin and age, one consisting of relatively young particles from nearby locations and one consisting of aged particles from western and central Europe. According to the height-resolved trajectories, the boundary between the different aerosol types was at about 900 and 1200 m at 1300 and 2100 UTC, respectively. Second, a comparison of lidar-derived and airborne measurements makes sense for height regions with similar air-mass history only. Parameters derived in the pollution layer at 1.2–2 km in the evening should be compared with values measured in situ in the height region from 2–3 km around noon, and parameters found for heights below 1200 m with the lidar should be compared to airborne measurements below 900 m. In addition, the relative humidity values at the two measurement times have to be checked for comparability because parameters such as particle size and refractive index strongly depend on particle growth with humidity.

#### 4.2.2. Lidar Measurements

[68] As already mentioned, multiwavelength lidar data for the inversion of physical particle properties were evaluated for the time period from 2020–2220 UTC on August 11, 1998. In Figure 8 a comparison of profiles of the particle backscatter coefficient at 532 nm and of the relative humidity for the times of the flight mission (Figure 8a) and of the evening measurement (Figure 8c) is given. Figure 8b shows the potential and equivalent potential temperatures determined with radiosondes at 1310 and 2246 UTC. The profiles confirm that no mixing occured between the aerosol layers of different origin.

[69] The lidar backscatter profiles shown in Figures 8a and 8c were evaluated with the Klett and with the Raman method, respectively. From the airborne in situ measurements, backscatter profiles for dry and ambient conditions were calculated on the basis of the measured dry size distribution (see Figure 8a). In the calculations, a value of 1.53 (ammonium sulfate) was used for the real part of the refractive index. The imaginary part was estimated to be 0.02 according to the soot content derived from the PSAP measurements. The humidity growth of the particles was estimated from the relative humidity measured with two radiosondes, that were launched at 1050 and at 1310 UTC, and from standard growth factors for ammonium sulfate [*Tang and Munkelwitz*, 1994]. The calculations were carried out in steps of 10% for humidity values from 40–70% and for 75% relative humidity. From the first sonde, only values below 2.6 km were used, because the sonde crossed a cloud and showed humidity values >85% above that height. After the humidity correction, one obtains a very good agreement of the in situ backscatter coefficient with the lidar values, which indicates the applicability of the humidity correction scheme. This finding is very important, because it justifies the use of standard growth factors in radiative-transfer models, which are applied to estimate the aerosol radiative forcing [*Wendisch et al*., 2002]. Furthermore, the strong sensitivity of the particle backscatter coefficient on the relative humidity becomes evident from the curves in Figure 8a.

[70] The humidity profile for the evening measurement

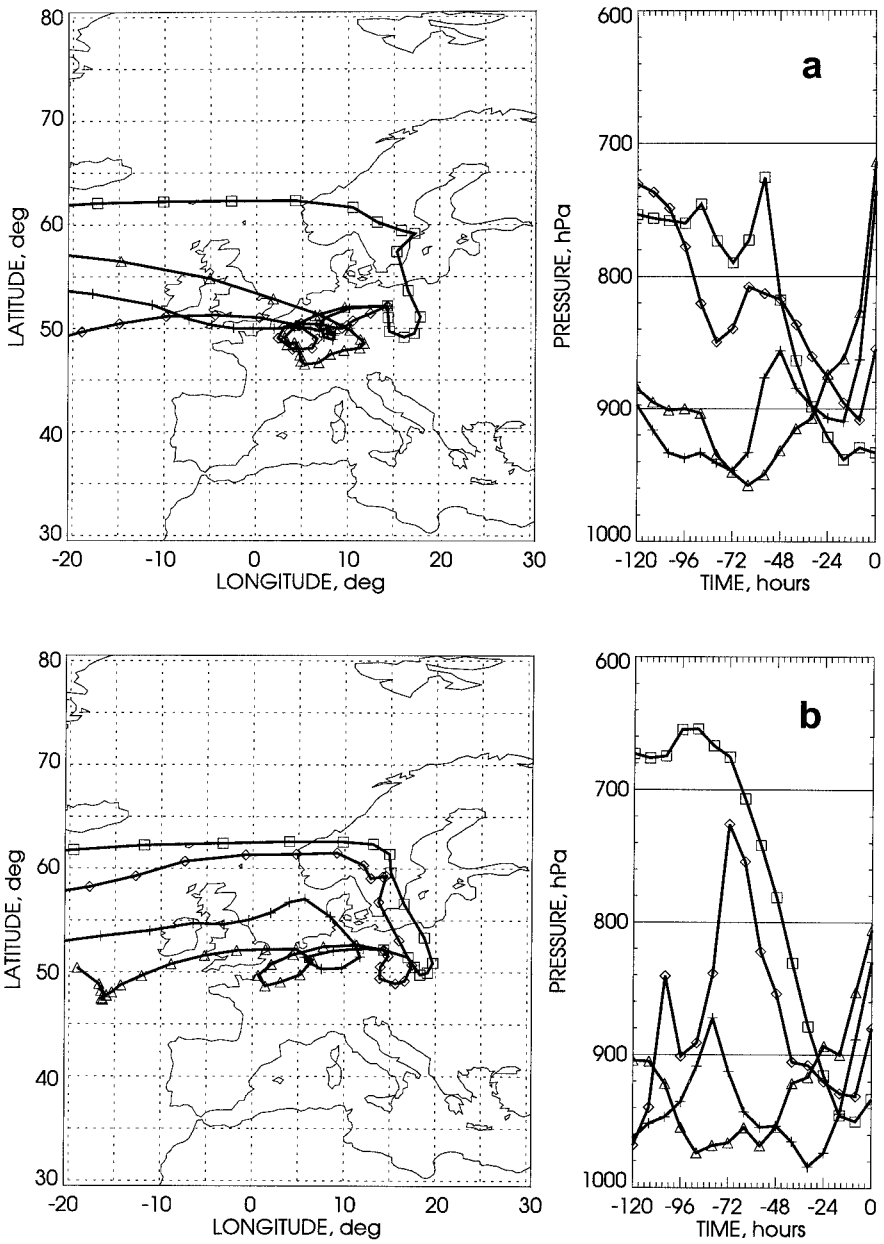


**Figure 7.** Five-day backward trajectories with arrival at Lindenberg on 11 August 1998 at (a) 1300 UTC and (b) 2100 UTC. The arrival heights above Lindenberg are (a) 645, 1395, 2645, and 2895 m and (b) 645, 1145, 1645, and 1895 m (right panels, time 0, from bottom to top).

shown in Figure 8c was derived from the water-vapor mixing ratio measured with the lidar and a radiosonde temperature profile. Again, a strong correlation between backscatter coefficient and relative humidity is found. The regions of strongest scattering and highest humidity at both measurement times (around 2.5 km in Figure 8a and around 1.6 km in Figure 8c) indicate the descending pollution layer, that arrived from western Europe. This layer was not influenced by the development of the local convective boundary layer at Lindenberg on that day as radiosonde and lidar observations showed.

[71] In Figure 8d the lidar ratios determined in the evening with the IfT multiwavelength lidar at 532 and at 355 nm and with the MPI UV lidar at 351 nm are shown. The MPI UV lidar was operated with XeF on that day (see section 2). Lidar ratios of approximately 50 and 60–65 sr were found at 532 and 351/355 nm, respectively, in the layer with maximum backscatter coefficient and highest humidity. From the measurements with the small telescope of the MPI UV lidar (see section 2), the lidar ratio at 351 nm could be derived from 500-m height upward. Higher values of the lidar ratio of about 75 sr were obtained in the lowermost heights.

[72] In Figure 9, profiles of backscatter and extinction coefficients are presented. Data from the IfT multiwavelength lidar and from the MPI UV lidar with a primary wavelength of 351 nm were available. The MPI water-vapor DIAL was not operated on that day. The measurements with the IfT multiwavelength lidar were taken under a zenith angle of 40°, so that, by applying the overlap correction in addition, profiles of

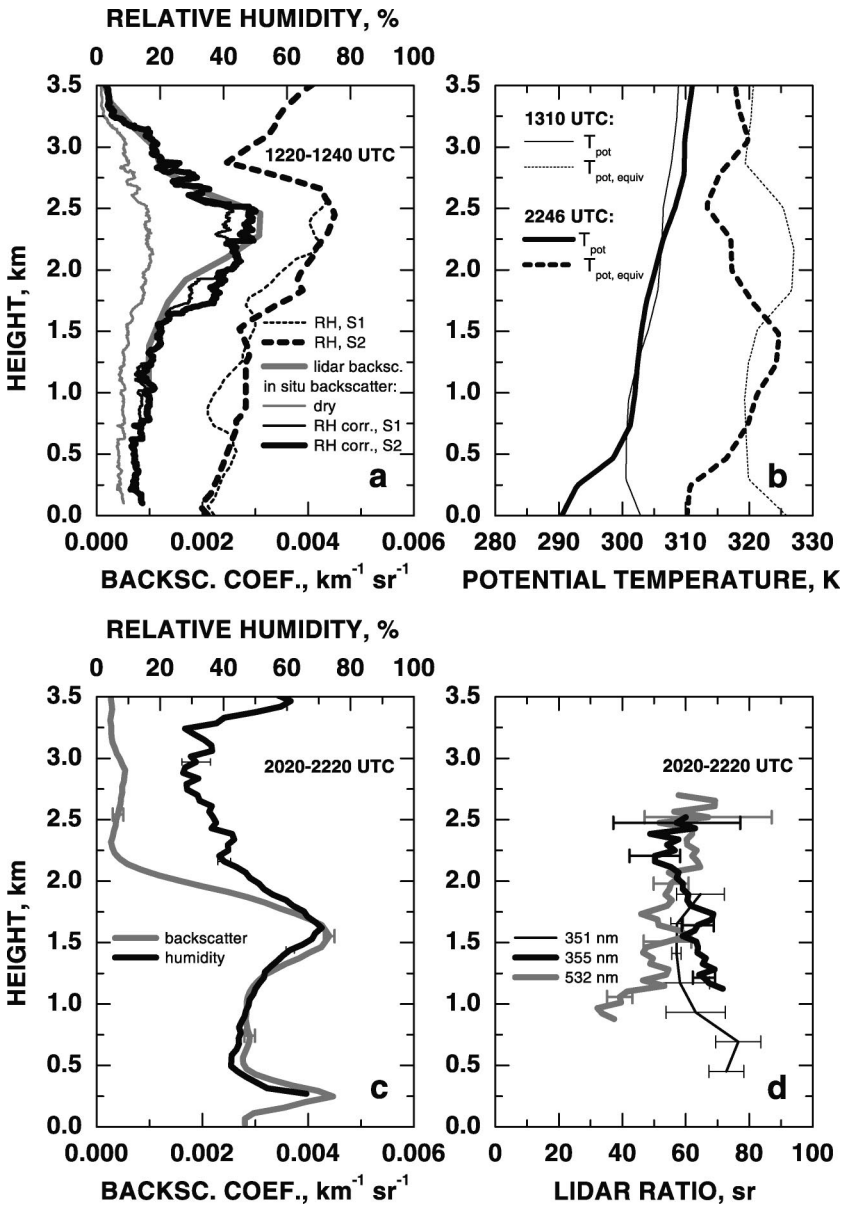


**Figure 8.** Measurement situation on 11 August 1998. (a) Particle backscatter coefficient at 532 nm determined with lidar after the Klett method with a height resolution of 180 m and calculated from airborne in situ measurements with a height resolution of ≈40 m. The humidity growth of the dry particles measured in situ was estimated from standard growth factors for ammonium sulfate and the relative humidity (RH) measured with radiosondes at 1050 UTC (sonde S1) and at 1310 UTC (sonde S2). (b) Potential and equivalent potential temperature determined with radiosondes for the two investigated periods. (c) Particle backscatter coefficient at 532 nm determined with lidar after the Raman method with a height resolution of 180 m and relative humidity from lidar water-vapor mixing ratio and radiosonde temperature with a height resolution of 184 and 230 m below and above 2000 m, respectively. The error bars indicate the statistical noise. (d) Lidar ratios at 351, 355, and 532 nm. The height resolution is 240 m (351 nm) and 180 m (355, 532 nm; 0–1200 m), 315 m (355, 532 nm; 1200–1800 m), 630 m (355, 532 nm; 1800–2160 m), and 900 m (355, 532 nm; above 2160 m). The error bars indicate the statistical noise.

backscatter coefficients with the Klett method and of extinction coefficients with the Raman method could be evaluated from 500- and 800-m height upward, respectively. The good agreement of the extinction profiles at 351 and 355 nm indicates that the near-field effects are appropriately considered. The backscatter profile at 355 nm of the IfT multiwavelength lidar could not be evaluated below 1200 m, because the signal was disturbed by detector overloading.

[73] The application of the Klett method for the evaluation of the elastic backscatter profiles is crucial in this case. As already explained, a high optical depth of the aerosol layer makes the solutions for the short wavelengths very sensitive to the lidar-ratio estimate. Also, an appropriate reference-value estimate is important for the longer wavelengths. For that reason, the mean value of the spectral optical depth measured with the star photometer [*Ansmann et al.*, 2002] during the

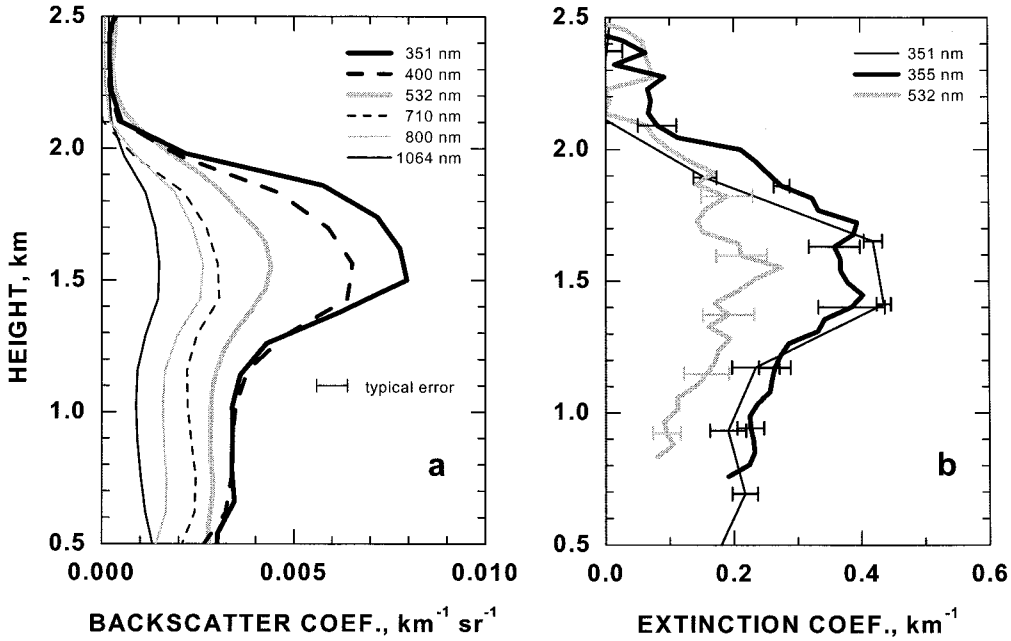


**Figure 9.** (a) Backscatter coefficients and (b) extinction coefficients measured in industrial-pollution aerosol at Lindenberg on 11 August 1998, between 2020 and 2220 UTC. The height resolution is 120 m (351 nm) and 138 m (400, 532, 710, 800, 1064 nm) for the backscatter coefficients and 240 m (351 nm) and 229 m (355, 532 nm) for the extinction coefficients. The error bars indicate statistical and systematic uncertainties.

time of the lidar measurement was used as an additional constraint. From the 532-nm backscatter profile determined with the Raman method down to the ground, it was estimated that the aerosol in the height range from 500–2200 m contributed about 65% to the column optical depth. The star photometer measurements from 444–863 nm revealed an Ångström coefficient of å = 1.57 for the wavelength dependence of the optical depth, $\delta \sim \lambda^{-å}$. The Ångström coefficient was used to interpolate the optical depth values (measured at 444, 532, 673, 779, and 863 nm) to the lidar wavelengths of 710 and 800 nm and to extrapolate them to 351, 355, 400, and 1064 nm. The input parameters for the Klett method were then chosen such, that the integrated backscatter coefficient for the height region from 500–2200 m multiplied by the chosen lidar ratio gave 65% of the optical depth value determined for the respective wavelength with the star photometer. According to the findings shown in Figure 8d, the mean lidar ratios were reduced from 60 to 40 sr from shorter to longer wavelengths.

[74] Figure 10 shows the spectral backscatter and extinction coefficients for the height regions from 1420–1700 m (peak, westerly flow) and from 900–1000 m (southeasterly flow). In Figure 10b the curves representing a wavelength dependence

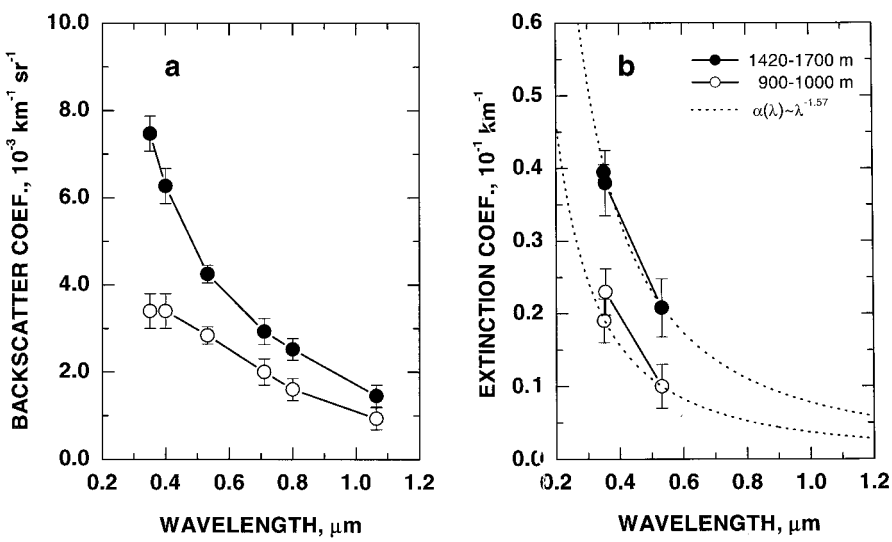


**Figure 10.** (a) Spectral backscatter coefficients and (b) spectral extinction coefficients for the height regions from 900–1000 m and from 1400–1720 m as derived from the profiles shown in Figure 9. The error bars indicate statistical and systematic uncertainties.

**Table 3.** Physical Particle Parameters From Inversion of Lidar Data Measured in the Height Region From 1420–1700 m on 11 August 1998, 2020–2220 UTC, and From in Situ Measurements of Particle Size Distributions Aboard the Partenavia Between 2000 and 2400 m at 1230 UTC

| | Lidar, Inversion | | Partenavia, in situ | |
|---|---|---|---|---|
| Parameter | IfT Algorithm | IMP Algorithm | Particles With $r \geq 50$ nm Dry | Particles With $r \geq 50$ nm 75% Humidity |
| $r_{eff}$, $\mu$m | 0.12±0.02 | 0.11±0.002 | 0.17±0.03 | 0.24±0.05 |
| $v_t$, $\mu m^3 cm^{-3}$ | 35±7 | 23±1 | 11±3 | 32±8 |
| $a_t$, $\mu m^2 cm^{-3}$ | 921±221 | 624±30 | 194±54 | 400±130 |
| $n_t$, $cm^{-3}$ | - | - | 858±56 | 858±56 |
| $m_{real}$ | 1.58±0.10 | 1.74±0.02 | (1.53) | (1.53) |
| $m_{imag}$ | 0.01±0.02 | 0.031±0.0001 | (0.02) | (0.02) |
| SSA (532 nm) | 0.94±0.06 | 0.87±0.01 | 0.91±0.02 | 0.91±0.02 |

of the extinction coefficient of $\alpha \sim \lambda^{-1.57}$ are shown for comparison. The extinction coefficients measured at 351, 355, and 532 nm in both height regions are well described by these curves. This finding supports the use of the spectral optical depth with the same wavelength dependence as a constraint in the calculation of the backscatter coefficients. Despite the fact of a similar wavelength dependence of the extinction coefficients in both height regions, the backscatter coefficients in the upper height show a steeper spectral slope than those in the lower height. Because the extinction-coefficient slope is more sensitive to the particle size, whereas the backscatter-coefficient slope or the ratio of extinction to backscattering is mainly determined by the chemical composition, this finding indicates a similar particle size but a different refractive index in the two height regions, which is confirmed by the inversion results given below.

#### 4.2.3. Inversion Results

[75] The inversion results for the measurements on 11 August 1998 are presented in Tables 3 and 4. Even though the trajectory analysis suggested a similar origin of the air masses for the two measurement times, one should be very careful in comparing the results here. Especially for the upper height interval, the dependence of the particle properties on relative humidity plays a major role. In Table 3 the airborne in situ parameters are shown for dry conditions and for a relative humidity of 75%. The respective humidity growth leads to an increase of the particle effective radius by a factor of 1.4, which results in an increase of the surface-area concentration by a factor of 2 and of the volume concentration by nearly a factor of 3. During the evening measurement the relative humidity in the investigated height region from 1420–1700 m was ~65% (see Figure 8c). Both inversion algorithms indicate that in the evening the particles of the descending pollution layer were smaller in size with an effective radius of about 0.12 $\mu$m. The IMP algorithm gives somewhat smaller radii as well as volume and surface-area concentrations than the IfT algorithm. The high uncertainties in the number and surface-area concentrations (for the number concentrations the respective errors were similar to the value itself, so that no number can be given at all) show the large influence of optically less active small particles on the inversion results (see subsection 4.1.3). It may be concluded that one has almost reached the limits for a successful inversion here, i.e., particle size distributions with an effective particle radius of the order of 0.1 $\mu$m and less are difficult to investigate.

[76] For the lower layer a better agreement is found for the effective radius derived from the inversion and from the in situ measurement. Again, comparably small particles with an effective radius of about 0.13 $\mu$m dominated the properties of the continental-pollution aerosol. Relative humidities of 40–50% were found for both measurement times in the lower layer, so that the sensitivity of the mircrophysical particle parameters on humidity growth is of less importance here. Higher concentrations are obtained from the inversion compared to the in situ measurements. This fact, however, is in accordance with the change of the absolute backscatter-coefficient values at 532 nm by a factor of 3 between the two measurement times (see Figures 8a and 8c) and is thus attributed to temporal and spatial inhomogeneity. Again, the uncertainties of the derived number concentrations are very large.

[77] For both height levels, real and imaginary parts of the refractive index are smaller than in the forest-fire layer. A higher single-scattering albedo follows. The IMP algorithm gives higher real parts than the IfT algorithm in this case. A comparison with the airborne values is not of great help here,

**Table 4.** Same as Table 3, but for Lidar Measurements From 900–1000 m and in Situ Measurements Between 500 and 900 m

| | Lidar, Inversion | | Partenavia, in Situ | |
|---|---|---|---|---|
| parameter | IfT Algorithm | IMP Algorithm | Particles With $r \geq 50$ nm Dry | Particles With $r \geq 50$ nm 40% Humidity |
| $r_{eff}$, $\mu$m | 0.13±0.02 | 0.10±0.03 | 0.14±0.01 | 0.16±0.01 |
| $v_t$, $\mu m^3 cm^{-3}$ | 29±3 | 18±1 | 5±1 | 7±1 |
| $a_t$, $\mu m^2 cm^{-3}$ | 696±38 | 616±45 | 100±19 | 131±20 |
| $n_t$, $cm^{-3}$ | 11193±6609 | 18455±5312 | 607±89 | 607±89 |
| $m_{real}$ | 1.48±0.03 | 1.62±0.02 | (1.53) | (1.53) |
| $m_{imag}$ | 0.008±0.003 | 0.008±0.003 | (0.02) | (0.02) |
| SSA (532 nm) | 0.94±0.02 | 0.95±0.02 | 0.90±0.02 | 0.91±0.02 |

because the refractive index for the calculations was only roughly estimated as explained above. For example, no change of the refractive index with humidity growth was considered. However, a real part of the refractive index of 1.53 is in good agreement with findings from the chemical analysis of particles at ground [*Ebert et al*., 2002], and the PSAP measurements give at least an estimate for the imaginary part.

#### 4.2.4. Discussion

[78] Small effective radii of 0.1–0.2 $\mu$m as found here are typical for particles from industrial pollution and were also found in other regions of the globe, e.g., in North America [*Remer et al*., 1997, 1999; *Tanré et al*., 1999] and above the Indian Ocean [*Müller et al*., 2000b, 2001b]. The particles showed a much stronger humidity growth than in the biomass-burning aerosol, which is in agreement with findings by *Kotchenruther and Hobbs* [1998]. Backscatter coefficients measured with lidar at 40% humidity were a factor of two higher than those calculated from the dry particle size distribution.

[79] The refractive index observed during the Tropospheric Aerosol Radiative Forcing Observational Experiment (TARFOX), which took place in the North Atlantic east of the United States, ranged from 1.40 to 1.53 in the real part and was lower than 0.017 in the imaginary part [*Russel et al*., 1999]. This experiment focused on the characterization of pollution from the highly industrialized east coast of the United States. Major contributor to the particles is sulfuric acid, which most likely is also the case for European pollution. Given the large uncertainty of the refractive indices in Table 3 and 4, similar values were found, except for the real part of the IMP algorithm.

[80] Single-scattering albedos were between 0.89 and 0.93 during TARFOX [*Russel et al*., 1999]. Shipborne in situ observations of aged continental air masses over the North Atlantic during ACE 2 showed a mean single-scattering albedo of $0.95 \pm 0.05$, with the lowest values being around 0.81 [*Quinn et al*., 2000]. Given the fact that ageing effects may cause an increase of this parameter, there is reasonable agreement with the values presented in Tables 3 and 4.

## 5. Conclusion

[81] A successful column closure experiment concerning the derivation of optical and microphysical particle parameters from multiwavelength-lidar and airborne in situ measurements was performed during LACE 98. Optical data were determined with up to four sophisticated lidar instruments, which measured particle backscatter and extinction coefficients at several wavelengths simultaneously and independently of each other. The data allowed detailed quality checks, which showed the consistency of the measurements. For the first time, extinction-coefficient profiles derived from Raman and high-spectral-resolution lidars could be compared, and excellent agreement was found.

[82] The optical data sets were inverted to particle microphysical properties with two different inversion algorithms. The results were compared with the respective parameters measured in situ. The two selected measurement cases of a biomass-burning aerosol layer and a industrial-polluted boundary layer covered highly different aerosol conditions and thus presented a rather strict benchmark test for the performance characteristics.

[83] In general, the two inversion algorithms gave reasonable values for the derived parameters of effective radius, volume and surface-area concentrations, refractive index, and single-scattering albedo. The particle number concentration, which is difficult to determine if a large number of small and thus optically less active particles is present, was reliable only when the effective radius of the size distribution was larger than about 0.2 $\mu$m. In the case of the forest-fire aerosol, very good agreement between the two algorithms and between inversion results and in situ measurements was found. The mean deviation of the results from the two algorithms was $<20\%$. In comparison to the in situ measurements, the inversion results deviated by $<30\%$ on average. Part of this difference could be attributed to the inhomogeneity of the aerosol layer. Larger discrepancies occured in the case of the polluted boundary layer. Remarkably lower volume concentrations and higher real parts of the refractive index were retrieved from the IMP algorithm than from the IfT algorithm.

[84] Further improvements of the inversion algorithms will address the observed shortcomings. Reasons for discrepancies between the algorithms may be a different processing of the errors of the optical data or the use of the regularization parameters. A different response of the algorithms may also occur, if a large amount of small particles influences the scattering properties of the aerosol as in the case of the polluted boundary layer on 11 August 1998. Another error source follows from the in situ measurements on 9 August 1998. These observations pointed toward an external rather than an internal mixture of particles. The inversion algorithms however use the constraint of a mean wavelength- and size-independent complex refractive index. This assumption may cause additional errors in the inversion results.

[85] In view of the comparison to the airborne measurements, the IfT algorithm showed reliable performance characteristics. For this reason, the technique is presently applied in the analysis of extensive sets of optical data obtained with the six-wavelength lidar during ACE 2 and INDOEX.

[86] **Acknowledgments.** LACE 98 was funded by the Bundesministerium für Bildung und Forschung within the aerosol research focus Aerosolforschungsschwerpunkt (AFS). We are very grateful to the scientific and technical staff of the Meteorological Observatory Lindenberg for the round-the-clock support during the experiment and for providing radiosonde and photometer data. ECMWF and Deutscher Wetterdienst admitted access to ECMWF data within the special project Validation of Trajectory Calculations.

## References

Ackermann, J., The extinction-to-backscatter ratio of tropospheric aerosol: A numerical study. *J. Atmos. Oceanic Techno.*, *15*, 1043–1050, 1998.

Althausen, D., D. Müller, A. Ansmann, U. Wandinger, H. Hube, E. Clauder, and S. Zörner, Scanning six-wavelength eleven-channel aerosol lidar, *J. Atmos. Oceanic Technol*., *17*, 1469–1482, 2000.

Anderson, B. E., et al., Aerosols from biomass burning over the tropical South Atlantic region: Distributions and impacts, *J. Geophys. Res*., *101*, 24,117–24,137, 1996.

Ansmann, A., M. Riebesell, and C. Weitkamp, Measurements of atmospheric aerosol extinction profiles with a Raman lidar, *Opt. Lett*., *15*, 746–748, 1990.

Ansmann, A., M. Riebesell, U. Wandinger, C. Weitkamp, and W. Michaelis, Independent measurement of extinction and backscatter profiles in cirrus clouds by using a combined Raman elastic-backscatter lidar, *Appl. Opt*., *29*, 3266–3272, 1992.

Ansmann, A., D. Althausen, U. Wandinger, K. Franke, D. Müller, F. Wagner, and J. Heintzenberg, Vertical profiling of the Indian aerosol plume with six-wavelength lidar during INDOEX: A first case study, *Geophys. Res. Lett*., *27*, 963–966, 2000.

Ansmann, A., F. Wagner, D. Althausen, D. Müller, A. Herber, and U. Wandinger, European pollution outbreaks during ACE 2: Lofted aerosol plumes observed with Raman lidar at the Portuguese coast, *J. Geophys. Res*., *106*, 20,725–20,734, 2001.

Ansmann, A., U. Wandinger, A. Wiedensohler, and U. Leiterer, Lindenberg Aerosol Characterization Experiment LACE 98: Overview, *J. Geophys. Res*., *107*, 10.1029/2000JD000233, 2002.

Böckmann, C., Hybrid regularization method for ill-posed inversion of multi-wavelength lidar data to retrieve aerosol size distribution, *Appl. Opt*., *40*, 1329–1342, 2001.

Böckmann, C., and J. Sarközi, The ill-posed inversion of multiwavelength lidar data by a hybrid method of variable projection, *Proc. SPIE Int. Soc. Opt. Eng*., *312*, 282–293, 1999.

Bohren, C. F., and D. R. Huffman, *Absorption and Scattering of Light by Small Particles*, 530 pp., John Wiley, New York, 1983.

Bösenberg, J., et al., The German Aerosol Lidar Network: Methodology, data, analysis, *Max Planck Rep*. *317*, Max Planck Inst. for Meteorol., Hamburg, Germany, 2001.

Busch, B., K. Kandler, L. Schütz, and C. Neusüß, Hygroscopic properties and water soluble fraction of atmospheric particles in the diameter range from 50 nm to 3.8 $\mu$m during the Aerosol Characterization Experiment in Lindenberg 1998, *J. Geophys. Res*., *107*, 10.1029/2000JD000228, 2002.

Cooney, J. A., J. Orr, and C. Tomasetti, Measurements separating the gaseous and aerosol components of laser atmospheric backscatter, *Nature*, *224*, 1098–1099, 1969.

Ebert, M., S. Weinbruch, A. Rausch, G. Gorzawski, G. Helas, P. Hoffmann, and H. Wex, Complex refractive index of aerosols during LACE 98 as derived from the analysis of individual particles, *J. Geophys. Res*., *107*, 10.1029/2000JD000195, 2002.

European Centre for Medium-Range Weather Forecasts (ECMWF), User guide to CCMWF products 2.1, *Meteorol. Bull. M3.2*, Reading, England, 1995.

Fernald, F. G., Analysis of atmospheric lidar observations: Some comments, *Appl. Opt*., *23*, 652–653, 1984.

Ferrare, R. A., S. H. Melfi, D. N. Whiteman, K. D. Evans, and R. Leifer, Raman lidar measurements of aerosol extinction and backscattering, 1, Methods and comparisons, *J. Geophys. Res*., *103*, 19,663–19,672, 1998a.

Ferrare, R. A., S. H. Melfi, D. N. Whiteman, K. D. Evans, M. Poellot, and Y. J. Kaufman, Raman lidar measurements of aerosol extinction and backscattering, 2, Derivation of aerosol real refractive index, single-scattering albedo, and humidifiction factor using Raman lidar and aircraft size distribution measurements, *J. Geophys. Res*., *103*, 19,673–19,689, 1998b.

Ferrare, R. A., et al., Comparison of aerosol optical properties and water vapor among ground and airborne lidars and Sun photometers during TARFOX, *J. Geophys. Res*., *105*, 9917–9933, 2000a.

Ferrare, R. A., et al., Comparison of LASE, aircraft, and satellite measurements of aerosol optical properties and water vapor during TARFOX, *J. Geophys. Res*., *105*, 9935–9947, 2000b.

Fiebig, M., A. Petzold, U. Wandinger, M. Wendisch, C. Kiemle, A. Stifter, M. Ebert, T. Rother, and U. Leiterer, Optical closure for an aerosol column: Method, accuracy, and inferable properties, applied to a biomass-burning aerosol and its radiative forcing, *J. Geophys. Res*., *107*, 10.1029/2000JD000192, 2002.

Forster, C., et al., Transport of boreal forest fire emissions from Canada to Europe, *J. Geophys. Res*., *106*, 22,887–22,906, 2001.

Golub, G. H., M. Heath, and G. Wahba, Generalized cross-validation as a method for choosing a good ridge parameter, *Technometrics*, *21*, 215–223, 1979.

Hobbs, P. V., J. S. Reid, R. A. Kotchenruther, R. J. Ferek, and R. Weiss, Direct radiative forcing by smoke from biomass burning, *Science*, *275*, 1776–1778, 1997.

Hsu, N. C., J. R. Herman, J. F. Gleason, O. Torres, and C. J. Seftor, Satellite detection of smoke aerosols over a snow/ice surface by TOMS, *Geophys. Res. Lett*., *26*, 1165–1168, 1999.

Kotchenruther, R. A., and P. V. Hobbs, Humidification factors of aerosols from biomass burning in Brazil, *J. Geophys. Res*., *103*, 32,081–32,089, 1998.

Lenoble, J., The particulate matter from biomass burning: A tutorial and critical review of its radiative impact, in *Global Biomass Burning: Atmospheric, Climatic, and Biospheric Implications*, edited by J. S. Levine, pp. 381–386, MIT Press, Cambridge, Mass., 1991.

Li, J., and J. Mao, Properties of atmospheric aerosols inverted from optical remote sensing, *Atmos. Environ., Part A*, *24*, 2517–2522, 1990.

Matthias, V., Vertikalmessungen der Aerosolextinktion und des Ozons mit einem UV-Raman-Lidar, Ph.D. dissertation, Univ. of Hamburg, Hamburg, Germany, 2000.

Melfi, S. H., Remote measurements of the atmosphere using Raman scattering, *Appl. Opt*., *11*, 1605–1610, 1972.

Müller, D., U. Wandinger, D. Althausen, I. Mattis, and A. Ansmann, Retrieval of physical particle properties from lidar observations of extinction and backscatter at multiple wavelengths, *Appl. Opt*., *37*, 2260–2263, 1998.

Müller, D., U. Wandinger, and A. Ansmann, Microphysical particle parameters from extinction and backscatter lidar data by inversion with regularization: Theory, *Appl. Opt*., *38*, 2346–2357, 1999a.

Müller, D., U. Wandinger, and A. Ansmann, Microphysical particle parameters from extinction and backscatter lidar data by inversion with regularization: Simulation, *Appl. Opt*., *38*, 2358–2368, 1999b.

Müller, D., F. Wagner, U. Wandinger, A. Ansmann, M. Wendisch, D. Althausen, and W. von Hoyningen-Huene, Microphysical particle parameters from extinction and backscatter lidar data by inversion with regularization: Experiment, *Appl. Opt*., *39*, 1879–1892, 2000a.

Müller, D., F. Wagner, D. Althausen, U. Wandinger, and A. Ansmann, Physical particle properties of the Indian aerosol plume derived from six-wavelength lidar observations on 25 March 1999 of the Indian Ocean Experiment, *Geophys. Res. Lett*., *27*, 1403–1406, 2000b.

Müller, D., K. Franke, F. Wagner, D. Althausen, A. Ansmann, and J. Heintzenberg, Vertical profiling of optical and physical particle properties over the tropical Indian Ocean with six-wavelength lidar, 1, Seasonal cycle, *J. Geophys. Res*., *106*, 28,567–28,575, 2001a.

Müller, D., K. Franke, F. Wagner, D. Althausen, A. Ansmann, and J. Heintzenberg, Vertical profiling of optical and physical particle properties over the tropical Indian Ocean with six-wavelength lidar, 2, Case studies, *J. Geophys. Res*., *106*, 28,577–28,595, 2001b.

Petzold, A., M. Fiebig, H. Flentje, A. Keil, U. Leiterer, F. Schröder, A. Stifter, M. Wendisch, and P. Wendling, Variability of aerosol properties relevant for radiative forcing observed at a continental site during LACE 98, *J. Geophys. Res*., *107*, 10.1029/2001JD001043, 2002.

Quinn, P. K., T. S. Bates, D. J. Coffman, T. L. Miller, J. E. Johnson, D. S. Covert, J. -P. Putaud, C. Neusüß, and T. Novakov, A comparison of aerosol chemical and optical properties from the 1st and 2nd Aerosol Characterization Experiments, *Tellus, Ser. B*, *52*, 239–257, 2000.

Radke, L. F., D. A. Heggs, J. H. Lyons, C. A. Brook, P. V. Hobbs, R. Weiss, and R. Rasmussen, Airborne measurements on smoke from biomass burning, in *Aerosols and Climate*, edited by P. V. Hobbs and M. P. McCormick, pp. 411–422, A. Deepak, Hampton, Va., 1988.

Redemann, J., R. P. Turco, R. F. Pueschel, M. A. Fenn, E. V. Browell, and W. B. Grant, A multi-instrument approach for characterizing the vertical structure of aerosol properties: Case studies in the Pacific Basin troposphere, *J. Geophys. Res*., *103*, 23,287–23,298, 1998.

Redemann, J., et al., Retrieving the vertical structure of the effective aerosol complex index of refraction from a combination of aerosol in situ and remote sensing measurements during TARFOX, *J. Geophys. Res*., *105*, 9949–9970, 2000.

Reid, J. S., and P. V. Hobbs, Physical and optical properties of young smoke from individual biomass fires in Brazil, *J. Geophys. Res*., *103*, 32,013–32,030, 1998.

Reid, J. S., P. V. Hobbs, R. J. Ferek, D. R. Blake, J. V. Martins, M. R. Dunlap, and C. Liousse, Physical, chemical, and optical properties of regional hazes dominated by smoke in Brazil, *J. Geophys. Res*., *103*, 32,059–32,080, 1998.

Remer, L. A., S. Gassó, D. A. Hegg, Y. J. Kaufman, and B. N. Holben, Urban/industrial aerosol: Ground-based Sun/sky radiometer and airborne in situ measurements, *J. Geophys. Res*., *102*, 16,849–16,859, 1997.

Remer, L. A., Y. J. Kaufman, B. N. Holben, A. M. Thompson, and D. McNamara, Biomass burning aerosol size distribution and modeled optical properties, *J. Geophys. Res*., *103*, 31,879–31,891, 1998.

Remer, L. A., Y. J. Kaufman, and B. N. Holben, Interannual variation of ambient aerosol characteristics on the east coast of the United States, *J. Geophys. Res*., *104*, 2223–2231, 1999.

Russel, P. B., J. M. Livingston, P. Hignett, S. Kinne, J. Wong, A. Chien, R. Bergstrom, P. Durkee, and P. V. Hobbs, Aerosol-induced radiative flux changes off the United States mid-Atlantic coast: Comparison of values calculated from Sun photometer and in situ data

with those measured by airborne pyranometer, *J. Geophys. Res*., *104*, 2289–2307, 1999.

Sasano, Y., and E. V. Browell, Light scattering characteristics of various aerosol types derived from multiple wavelength lidar observations, *Appl. Opt*., *28*, 1670–1679, 1989.

Stohl, A., G. Wotawa, P. Seibert, and H. Kromp-Kolb, Interpolation errors in wind fields as a function of spatial and temporal resolution and their impact on different types of kinematic trajectories, *J. Appl. Meteorol*., *34*, 2149–2165, 1995.

Tang, I. N., and H. R. Munkelwitz, Composition and temperature dependence of the deliquescence properties of hygroscopic aerosols, *Atmos. Environ., Part A*, *27*, 467–473, 1994.

Tanré, D., L. A. Remer, Y. J. Kaufman, S. Mattoo, P. V. Hobbs, J. M. Livingston, P. B. Russell, and A. Smirnov, Retrieval of aerosol optical thickness and size distribution over ocean from the MODIS airborne simulator during TARFOX, *J. Geophys. Res*., *104*, 2261–2278, 1999.

Wendisch, M., et al., Aerosol-radiation interaction in the cloudless atmosphere during LACE 98, 1, Measured and calculated solar and spectral surface insolations, *J. Geophys. Res*., *107*, 10.1029/2000JD000226, 2002.

Wulfmeyer, V., and J. Bösenberg, Ground-based differential absorption lidar for water-vapor profiling: Assessment of accuracy, resolution, and meteorological applications, *Appl. Opt*., *37*, 3825–3844, 1998.

Yamasoe, M. A., Y. J. Kaufman, O. Dubovik, L. A. Remer, B. N. Holben, and P. Artaxo, Retrieval of the real part of the refractive index of smoke particles from Sun/sky measurements during SCAR-B, *J. Geophys. Res*., *103*, 31,893–31,902, 1998.

---

D. Althausen, A. Ansmann, D. Müller, U. Wandinger, and M. Wendisch, Institut für Troposphärenforschung, Permoserstr. 15, 04318 Leipzig, Germany. (dietrich@tropos.de; albert.ansmann@tropos.de; detlef@tropos.de; ulla@tropos.de; wendisch@tropos.de)

C. Böckmann, Institut für Mathematik, Universität Potsdam, Postfach 601553, 14415 Potsdam, Germany. (bockmann@rz.uni-potsdam.de)

J. Bösenberg and V. Matthias, Max-Planck-Institut für Meteorologie, Bundesstr. 55, 20146 Hamburg, Germany. (boesenberg@dkrz.de; matthias@dkrz.de)

M. Fiebig and V. Weiß, Institut für Physik der Atmosphäre, Deutsches Zentrum für Luft- und Raumfahrt, Oberpfaffenhofen, 82234 Wessling, Germany. (markus.fiebig@dlr.de)

A. Stohl, Lehrstuhl für Bioklimatologie und Immissionsforschung, Technische Universität München, Am Hochanger 13, 85354 Freising-Weihenstephan, Germany. (as@atmosl.met.forst.uni-muenchen.de)

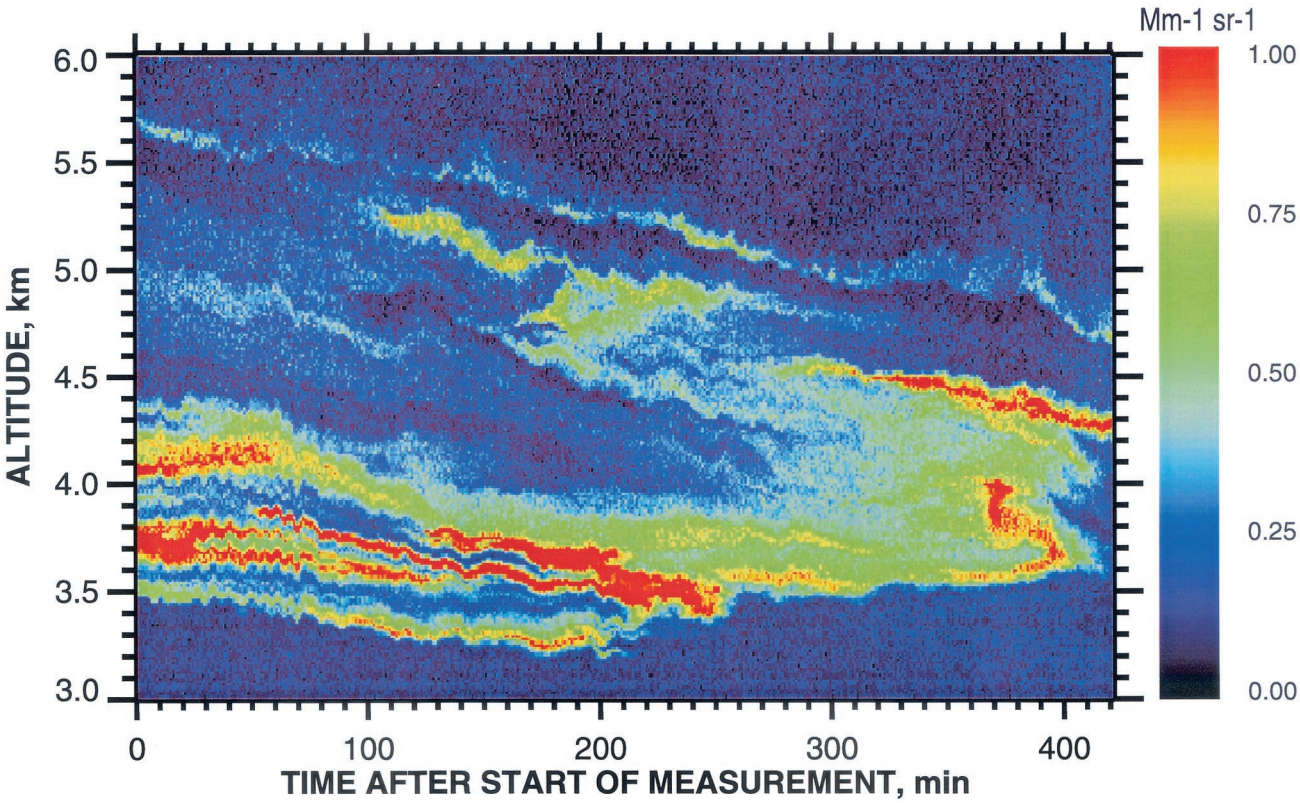


**Figure 1.** Backscatter coefficient at 532 nm in the biomass-burning aerosol layer from 2000 UTC on 9 August to 0300 UTC on 10 August 1998. The measurement was taken with the IfT multiwavelength lidar. The resolution is 15 m in height and 30 s in time.